ELSEVIER

Contents lists available at ScienceDirect

## Applied Catalysis B: Environment and Energy

journal homepage: www.elsevier.com/locate/apcatb



# Encapsulation of perovskite quantum dots in dual-metal sites metal-organic frameworks for efficient artificial photosynthesis

Jing-Jing Wang <sup>a,b,1</sup>, Hong-Juan Wang <sup>a,1</sup>, Yun-Nan Gong <sup>a,\*</sup>, Jing-Yi Liu <sup>a</sup>, Chong-Jiu Lu <sup>a</sup>, Hao-Yu Yang <sup>a</sup>, Di-Chang Zhong <sup>a,\*</sup>, Tong-Bu Lu <sup>a,\*</sup>

#### ARTICLE INFO

#### Keywords: Metal-organic frameworks ·CO<sub>2</sub> photoreduction Dual-metal sites Synergistic catalysis Artificial photosynthesis

#### ABSTRACT

Metal-organic frameworks (MOFs) have sparked interest in photocatalysis. Unfortunately, they usually exhibit insufficient charge separation and catalytic efficiencies for artificial photosynthesis. Herein, the encapsulation of CsPbBr<sub>3</sub> quantum dots (QDs) into the pores of dual-metal sites MOFs (MOF-919-Cu<sub>2</sub>M, M = Cu, Co, Co, Co) has been achieved to fabricate a series of CsPbBr<sub>3</sub>@MOF-919-Cu<sub>2</sub>M heterojunctions for Co<sub>2</sub> photoreduction to HCOOH coupled with  $H_2O$  oxidation to  $O_2$ . The close contact of CsPbBr<sub>3</sub> QDs and MOF-919-Cu<sub>2</sub>M shortens the photo-induced electron transfer distance, which dramatically facilitates the charge separation. Meanwhile, the Cu and Co dual-metal sites within the Cu<sub>2</sub>M clusters exhibit synergistic catalysis effect, which significantly enhances catalytic efficiency of active sites. As a result, CsPbBr<sub>3</sub>@MOF-919-Cu<sub>2</sub>Co achieves the highest photocatalytic performance with an electron consumption rate of CsPbBr<sub>3</sub>@MOF-919-Cu<sub>2</sub>Co achieves the highest photocatalytic mixture of CsPbBr<sub>3</sub> QDs, csPbBr<sub>3</sub> QD

## 1. Introduction

The large-scale usage of fossil fuels leads to the excessive emissions of carbon dioxide (CO<sub>2</sub>) into the atmosphere, which has caused serious environmental issue [1,2]. More and more countries have proposed the carbon neutral schedule. The exploration of effective strategies for  $\rm CO_2$  conversion is an urgent need. Inspired by natural photosynthesis, the conversion of  $\rm CO_2$  and  $\rm H_2O$  into value-added fuels and  $\rm O_2$  using sunlight is regarded as a potential solution to achieve carbon neutral goal [3–5]. However, achieving this overall reaction with high efficiency is still challenging owing to the high chemical inertness of both  $\rm CO_2$  and  $\rm H_2O$  molecules, as well as multielectron and multiproton transfer processes for both  $\rm CO_2$  reduction and  $\rm H_2O$  oxidation reactions [6–11]. Therefore, the development of efficient photocatalysts to realize the artificial photosynthesis is highly desirable.

Metal-organic frameworks (MOFs), as a class of crystalline porous material, which are constructed by metal ions/clusters and organic ligands, have demonstrated great potential in artificial photosynthesis due to their periodic and tailorable structures, high surface area, semiconductor-like behavior and well-exposed active sites, etc [12–16]. Nevertheless, they usually exhibit insufficient charge separation and catalytic efficiencies, and thus poor photocatalytic performance. Over the past several decades, various strategies have been developed to improve catalytic activity for MOF-based photocatalytsts. Among them, the construction of composite photocatalysts by integrating semiconductors and MOFs is considered to be an effective strategy as the charge separation efficiency of composites can be significantly enhanced over single component [17-24]. In particular, the encapsulation of semiconductors in the pores of MOFs to form composite photocatalysts has attracted more and more attentions because the photo-induced electron transfer distance between MOFs and semiconductors can be dramatically shortened compared with their simply physical mixture, thus can further boost charge separation efficiency [23,24].

In addition to increasing charge separation efficiency, a series of

E-mail addresses: yngong@email.tjut.edu.cn (Y.-N. Gong), dczhong@email.tjut.edu.cn (D.-C. Zhong), lutongbu@tjut.edu.cn (T.-B. Lu).

 <sup>&</sup>lt;sup>a</sup> Institute for New Energy Materials and Low Carbon Technologies, School of Materials Science and Engineering, Tianjin University of Technology, Tianjin 300384, China
<sup>b</sup> College of Biological and Chemical Engineering, Qilu Institute of Technology, Jinan 250200, China

<sup>\*</sup> Corresponding authors.

 $<sup>^{1}\,</sup>$  Authors made equal contributions.

dual-metal sites MOFs with appropriate  $M\cdots M$  separations have been designed and fabricated to enhance catalytic efficiency via the dinuclear metal synergistic catalysis (DMSC) effect. In photocatalytic  $CO_2$  reduction reaction,  $CO_2$  adsorption and activation are two important steps with high reaction energy barriers, which may determine the reactive dynamics. For dual-metal sites MOFs, two metal centers can bind a  $CO_2$  molecule simultaneously with bridge mode to promote the activation of  $CO_2$  molecule, which can lower the reaction energy barriers of the rate-determining step compared with the single-metal site counterparts [25–27]. In this context, the regulation of dual-metal sites of MOFs is expected to modulate dual-metal synergistic effect to further boost catalytic efficiency for  $CO_2$  photoreduction, while the related report has not been documented so far. Therefore, it is meaningful to encapsulate semiconductors in the pores of MOFs and regulate dual-metal sites of MOFs to improve both charge separation and catalytic efficiencies.

Based on the above in mind, we rationally constructed three  $CsPbBr_3@MOF-919-Cu_2M$  (M = Cu, Co, Zn) heterojunction photocatalysts by encapsulating  $CsPbBr_3$  quantum dots (QDs) in the pores of dual-metal sites  $MOF-919-Cu_2M$  for visible-light-driven  $CO_2$  reduction to HCOOH coupled with  $H_2O$  oxidation to  $O_2$ . The close contact of  $CsPbBr_3$  QDs and  $MOF-919-Cu_2M$  shortens the photo-induced electron transfer distance, thus greatly enhances charge separation efficiency. Meanwhile, the Cu and M dual-metal sites within the  $Cu_2M$  clusters exhibit synergistic catalysis effect, which significantly enhances catalytic efficiency of active sites. Among which, the Cu and Co dual-metal sites of  $CsPbBr_3@MOF-919-Cu_2Co$  show the optimal synergistic effect due to the strongest binding strength between Cu/Co and  $HCOO^*$  intermediate, resulting in the highest catalytic activity for photocatalytic  $CO_2$  reduction to HCOOH.

## 2. Experimental section

## 2.1. Materials and equipments

All chemicals were purchased from commercial sources and used without further purification. Powder X-ray diffraction (XRD) were collected on D8 ADVANCEX-Ray Diffractometers with Cu K $\alpha$  radiation  $(\lambda = 1.54 \text{ Å})$ . Transmission electron microscopy (TEM), high-resolution TEM (HRTEM) and energy dispersive spectroscopic (EDS) mapping were acquired on transmission electron microscope with a LaB6 Gun (Tecnai G2 Spirit TWIN and Talos F200 X, FEI, USA) at an acceleration voltage of 120 kV. Gas sorption measurements were conducted using a multistation specific surface micropore and vapor adsorption analyzer (BEL-SORP-Mas, Microtrac BEL, Japan). X-ray photoelectron spectroscopy (XPS) spectra were carried out using an X-ray spectrometer (ESCALAB 250 Xi spectrometer, Thermo Scientific, USA) with Al Kα as the excitation source. Solid-state UV-vis absorption spectra were obtained on a UV-vis spectrophotometer (UV-3600, Shimadzu, Japan). Photoluminescence (PL) spectra were measured with an F-4600 fluorescence spectrometer. Time-resolved PL (TRPL) spectra were acquired on an FLS1000 fluorescence spectrometer. Electron paramagnetic resonance (EPR) spectra were collected on EMXplus-6/1 and JEOL JES-FA200 EPR spectrometers. In situ fourier transform infrared spectroscopy (FTIR) spectra were recorded on Nicolet iS50 IR spectrometers, and samples were tableted with KBr as support. The contents of metals were quantified by inductively coupled plasma mass spectrometry (ICP-MS) (iCAP RQ, Germany). Transient absorption (TA) spectra were measured on the LP980 laser flash photolysis instrument (Edinburgh). The catalytic product in gaseous phase of the reaction system was analyzed by gas chromatography (GC-2014 +ATF, 230 C, Shimadzu, Japan) equipped with two automated gas sampling valves, which contain a thermal conductivity detector (TCD) and a flame ionization detector (FID). The liquid products were analyzed using ion chromatography (Eco IC) and nuclear magnetic resonance (NMR, Bruker AVANCE AV III 400) spectroscopy. The isotopes of <sup>18</sup>O for O<sub>2</sub> were analyzed using mass spectrometry (HPR-20 QIC). Photocurrent, electrochemical impedance spectroscopy (EIS), Mott-Schottky plots, electrochemical active surface areas (ECSA), cyclic voltammetry (CV) and linear sweep voltammetry (LSV) measurements were performed on CHI 660E and CHI 760E electrochemical workstations.

## 2.2. Synthesis of MOF-919-Cu<sub>2</sub>M

MOF-919-Cu<sub>3</sub> was synthesized according to the literature [28]. Typically, ScCl<sub>3</sub>·6 H<sub>2</sub>O (76.2 mg), Cu(NO<sub>3</sub>)<sub>2</sub>·3 H<sub>2</sub>O (135.6 mg), 1H-pyr-azole-4-carboxylic acid (H<sub>2</sub>PyC, 34.8 mg) and *N*,*N*-dimethylformamide (DMF) (10 mL) were added in a 20 mL Pyrex vial, which was heated at 100 °C for 15 h. After cooling to room temperature, the green product was collected by filtration, immersed in DMF for 3 days, and followed in ethanol for 3 days. The product was dried under vacuum at 60 °C for 12 h to yield MOF-919-Cu<sub>3</sub>. Then, 20 mg MOF-919-Cu<sub>3</sub> was added in 5.0 mL 0.5 M DMF solution of Zn(NO<sub>3</sub>)<sub>2</sub>·6 H<sub>2</sub>O or Co(NO<sub>3</sub>)<sub>2</sub>·6 H<sub>2</sub>O, which was heated at 90 °C for 24 h to yield gray product of MOF-919-Cu<sub>2</sub>Zn or dark gray product of MOF-919-Cu<sub>2</sub>Co. Afterwards, MOF-919-Cu<sub>2</sub>Zn and MOF-919-Cu<sub>2</sub>Co were soaked in DMF and ethanol respectively for 3 days, filtrated and dried under vacuum at 60 °C for 12 h. Finally, MOF-919-Cu<sub>2</sub>M (M = Cu, Zn, Co) were further dried under vacuum at 150 °C for 12 h to yield the activated MOF-919-Cu<sub>2</sub>M.

## 2.3. Preparation of CsPbBr<sub>3</sub>@MOF-919-Cu<sub>2</sub>M

20~mg activated MOF-919-Cu $_2M$  was dispersed in 5.0~mL 0.005-0.016~M DMF solution of  $PbBr_2$ , and stirred for 2~h. The  $PbBr_2@MOF-919-Cu_2M$  were collected by filtration and washing with a mixed solvent of DMF/ethanol (v:v =1:1). Afterwards,  $PbBr_2@MOF-919-Cu_2M$  was dispersed in 1.0~mL toluene. On the other hand, 21.3~mg CsBr was dispersed in 10~mL methanol and stirred at  $60~^{\circ}C$  for 1~h. Then, 1.0~mL CsBr methanolic solution was added quickly to the toluene solution of  $PbBr_2@MOF-919-Cu_2M$ , and stirred at room temperature for 5~min. The CsPbBr $_3@MOF-919-Cu_2M$  were collected by filtration and washing with n-hexane for five times.

## 2.4. Preparation of CsPbBr<sub>3</sub>@MOF-919-Cu<sub>x</sub>Co<sub>v</sub>

The  $CsPbBr_3@MOF-919-Cu_xCo_y$  with different atomic ratios of Cu: Co were prepared following the same procedure as  $CsPbBr_3@MOF-919-Cu_2Co$  except for the different exchange time (Table S1).

## 2.5. Synthesis of CsPbBr<sub>3</sub> QDs

A mixture of  $Cs_2CO_3$  (0.41 g), octadecene (ODE, 20 mL) and oleic acid (OA, 1.3 mL) was added in a 50 mL three-neck flask, and heated at 120 °C in Ar atmosphere for 1 h, followed at 150 °C for 30 min to yield Cs-OA solution. Moreover, a mixture of PbBr<sub>2</sub> (0.70 g), ODE (50 mL), oleylamine (OM, 5.0 mL) and OA (5.0 mL) was added in a 250 mL three-neck flask, heated at 120 °C in Ar atmosphere for 1 h, followed by heating at 170 °C for 10 min. Then, 4.0 mL of prepared Cs-OA solution was swiftly added, followed by cooling in liquid nitrogen. The yellow precipitate was obtained by centrifuging and washing with ethyl acetate for three times, followed by washing with hexane to remove aggregated particles. Finally, the CsPbBr<sub>3</sub> QDs was obtained by filtration and washing with ethyl acetate.

#### 2.6. XAS measurements

The X-ray absorption spectroscopy (XAS) measurements were carried out on the sample at 21 A X-ray nano diffraction beamline of Taiwan Photon Source (TPS), National Synchrotron Radiation Research Center (NSRRC). This beamline adopted 4-bounce channel-cut Si (111) monochromator for mono-beam X-ray nanodiffraction and X-ray absorption spectroscopy. The end-station equipped with three ionization chambers and Lytle/SDD detector after the focusing position of KB mirror for

transmission and fluorescence mode X-ray absorption spectroscopy. The photon flux on the sample is range from  $1\times10^{11} \sim 3\times10^9$  photon/sec for X-ray energy from 6 to 27 keV.

## 2.7. Photocatalytic experiments

The photocatalytic CO $_2$  reduction measurements were carried out in a 16 mL sealed Pyrex bottle. 1.0 mg catalyst, 5 mL acetonitrile and 20  $\mu L$  deionized water were added in the sealed Pyrex bottle, degassed with CO $_2$  to remove O $_2$  and other gases, followed by a 300 W Xe lamp irradiation with a 420 nm filter (light intensity, 80 mW cm $^{-2}$ ). The generated gaseous products were analyzed by gas chromatography, and liquid products were analyzed by NMR spectroscopy and ion chromatography.

## 2.8. AQE measurements

The apparent quantum efficiency (AQE) was measured in an identical experimental condition as photocatalytic  $\mathrm{CO}_2$  reduction except for the incident light resource. The catalytic system was irradiated by light emitting diode (LED) light for 1 h with wavelengths of 395, 425 and 450 nm, respectively (80 mW cm<sup>-2</sup>, irradiation area 0.8 cm<sup>2</sup>). The generated products were quantitatively detected by ion chromatography. The value of AQE was calculated by the below expression:

$$AQE = \frac{Total \ number \ of consumed electrons}{Total \ number \ of incident electrons}$$

#### 2.9. Photoelectrochemical measurements

Photocurrent, EIS and Mott-Schottky plots measurements were performed using a three-electrode system in 0.1 M tetrabutylammonium hexafluorophosphate acetonitrile/water (v:v = 100:1) solution. The working electrode was prepared by depositing 1.0 mg photocatalyst on the surface of fluorine-doped tin oxide (FTO,  $0.5 \times 0.5 \text{ cm}^2$ ). Pt plate and Ag/AgCl were used as the counter electrode and reference electrodes, respectively. Photocurrent measurements were recorded at -0.4 V (light intensity, 80 mW cm<sup>-2</sup>). EIS measurements were carried out at -0.6 V in the dark. Mott-Schottky plots were recorded at frequencies of 300, 600 and 900 Hz, respectively. CV and LSV measurements were performed using a three-electrode system in acetonitrile/ water (v:v = 4:1) solution. Pt silk and Ag/AgNO<sub>3</sub> (0.1 M) were used as the counter electrode and reference electrodes, respectively. For CV measurements, the working electrode was prepared by depositing 40 µg photocatalyst on the surface of glassy carbon electrode. For LSV measurements, the working electrode was prepared by depositing 1.0 mg photocatalyst on the surface of FTO  $(0.5 \times 0.5 \text{ cm}^2)$ .

## 2.10. TA spectra measurements

 $1.0~mg~CsPbBr_3@MOF-919-Cu_2M~was~dispersed~in~3.0~mL~acetonitrile, which was degassed with Ar to remove <math display="inline">O_2$  and other gases. The TA spectra measurements were carried out at room temperature.

## 2.11. In situ FTIR spectra experiments

A mixture of 1.0 mg CsPbBr $_3$ @MOF-919-Cu $_2$ M and 50 mg KBr was ground for 10 min. Then the mixture was sealed in the chamber for purging with N $_2$  for 20 min. The *in situ* FTIR spectra were collected under light irradiation with the incremental time upon the introduction of a mixture of CO $_2$ /CH $_3$ CN/H $_2$ O vapour.

## 2.12. Lifetime analysis

The average lifetime of the excited state  $(\tau_{Ave} = \Sigma \tau_i A_i)$  was obtained by fitting the TRPL spectra with the triple exponential decay function  $(I_{PL} = A_0 + A_1 exp(t/\tau_1) + A_2 exp(-t/\tau_2) + A_3 exp(-t/\tau_3)$  (where  $A_i$ 

represents the amplitude coefficient and  $\tau_i$  represents the lifetime). Here, three components were used to analyze the average lifetimes of CsPbBr3, CsPbBr3@MOF-919-Cu2M and CsPbBr3/MOF-919-Cu2M, namely,  $\tau_{Ave}=\tau_1A_1+\tau_2A_2+\tau_3A_3$  ( $A_1+A_2+A_3=1$ ).

#### 2.13. DFT calculations

The spin-polarized density functional theory (DFT) calculations were performed based on the Vienna ab initio simulation package (VASP) [29]. The generalized gradient approximation (GGA) in the form of Perdew-Burke-Ernzerh (PBE) [30] functional was applied to describe the exchange-correlation interaction. The projected augmented wave (PAW) method [31] was used to describe the electron-ion interaction. And the electron wave functions were expanded by a plane wave basis set with an energy cutoff of 400 eV. In addition, the DFT-D3 method was applied to describe the van der Waals interactions. The convergence criteria for the energy and residual force were set to  $10^{-5}$  eV and 0.03 eV/Å, respectively. During the calculations, the Brillouin zone integration was carried out with a single gamma point. The Gibbs free energy of each species in the simulated pathway was calculated as follows:

$$G = E_{DFT} + E_{ZPE} + \int C_V dT - TS$$

Where  $E_{DFT}$  is the electronic energy directly obtained from DFT calculations,  $E_{ZPE}$  is the zero-point vibrational energy,  $\int C_V dT$  is the heat capacity, T is the temperature (298.15 K), and S is the entropy (Tables S2 and S3).

#### 3. Results and discussion

## 3.1. Synthesis and characterization

MOF-919-Cu<sub>3</sub> with Cu<sub>3</sub> cluster was first synthesized according to the reported procedure [28]. The powder XRD pattern of MOF-919-Cu<sub>3</sub> is basically identical to its simulated one, demonstrating the high phase purity (Fig. 1a). The N<sub>2</sub> adsorption isotherm of MOF-919-Cu<sub>3</sub> shows a reversible type IV isotherm with the saturated N<sub>2</sub> uptake of 593.9 cm<sup>3</sup> g<sup>-1</sup> (STP) and the corresponding Brunauer-Emmett-Teller (BET) surface area of 1061.3 m<sup>2</sup> g<sup>-1</sup> (Fig. S1). Moreover, MOF-919-Cu<sub>3</sub> shows three types of pores with the sizes of about 2.0, 3.4 and 5.7 nm respectively, which are in agreement with its crystal structure (Figs. S2 and S3). Afterwards, MOF-919-Cu<sub>2</sub>Co and MOF-919-Cu<sub>2</sub>Zn were prepared through ion exchange strategy, in which MOF-919-Cu<sub>3</sub> was immersed in DMF containing Co(NO<sub>3</sub>)<sub>2</sub>·6 H<sub>2</sub>O and Zn(NO<sub>3</sub>)<sub>2</sub>·6 H<sub>2</sub>O respectively at 90 °C [32]. Taking MOF-919-Cu<sub>x</sub>Co<sub>y</sub> as a representative (x and y represent the amounts of Cu and Co, respectively), the ICP-MS measurements show that the content of Co increases along with the incremental soaking time, and the atomic ratio of Cu:Co is 2:1 at the soaking time of 24 h (Table S1), with the color change from green to dark gray (Fig. S4). Additionally, the results of DFT calculations demonstrate that the exchange energy for the exchange of the first Cu in Cu3 cluster with Co  $(Cu_3 + Co \rightarrow Cu_2Co + Cu, -0.45 \text{ eV})$  is lower than those for the second (0.14 eV) and third (0.15 eV) ones, revealing that it prefers to form Cu<sub>2</sub>Co cluster during the process of ion exchange [33,34]. All the above results indicate that one Cu in the Cu<sub>3</sub> cluster prefers to be exchanged by one Co to form a Cu<sub>2</sub>Co cluster in MOF-919-Cu<sub>2</sub>Co at the soaking time of 24 h.

Powder XRD pattern, N<sub>2</sub> adsorption isotherm and pore size distribution of MOF-919-Cu<sub>2</sub>Co are similar to those of MOF-919-Cu<sub>3</sub> (Figs. 1a, S1 and S2), demonstrating that its crystallinity and porous structure are well kept. To elucidate the microstructural information of Co in MOF-919-Cu<sub>2</sub>Co, XAS was carried out. As shown in Fig. 1b, the Fourier transform-extended X-ray absorption fine structure (FT-EXAFS) spectrum of MOF-919-Cu<sub>2</sub>Co for Co exhibits a prominent peak at 1.51 Å, corresponding to the Co-N/O scattering paths. No Co-Co scattering path

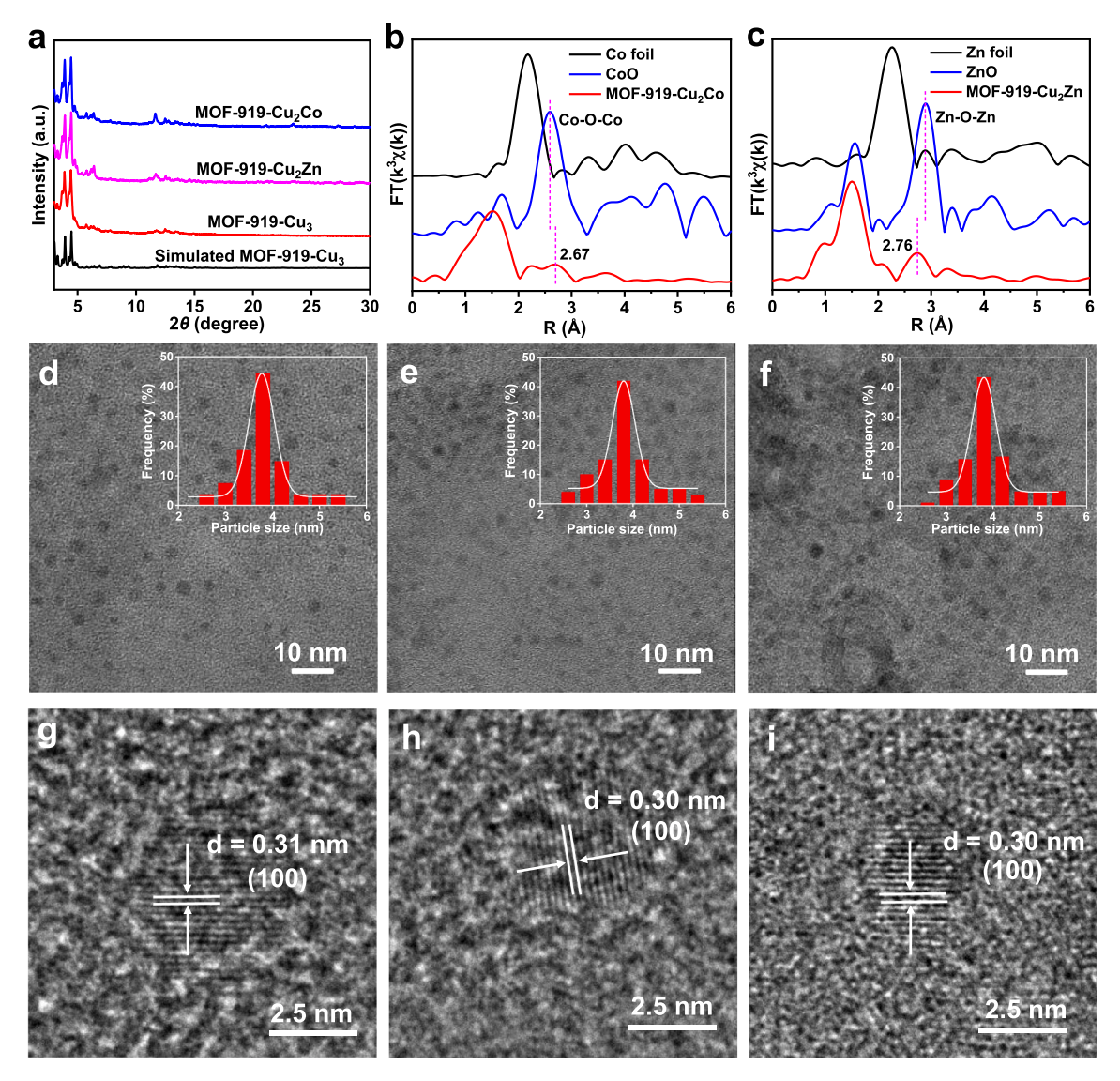


Fig. 1. (a) Powder XRD patterns of the synthesized MOF-919-Cu<sub>2</sub>Xn and MOF-919-Cu<sub>2</sub>Co, and simulated MOF-919-Cu<sub>3</sub>. (b) Co K-edge EXAFS spectra of Co foil, CoO and MOF-919-Cu<sub>2</sub>Co at R space. (c) Zn K-edge EXAFS spectra of Zn foil, ZnO and MOF-919-Cu<sub>2</sub>Zn at R space. (d-f) TEM images of CsPbBr<sub>3</sub>@MOF-919-Cu<sub>3</sub> (d), CsPbBr<sub>3</sub>@MOF-919-Cu<sub>2</sub>Co (e) and CsPbBr<sub>3</sub>@MOF-919-Cu<sub>2</sub>Zn (f), the black dots are CsPbBr<sub>3</sub> QDs. Inset: the particle size distribution of CsPbBr<sub>3</sub> QDs. (g-i) HRTEM images with lattice fringes of CsPbBr<sub>3</sub> QDs in CsPbBr<sub>3</sub>@MOF-919-Cu<sub>2</sub> (g), CsPbBr<sub>3</sub>@MOF-919-Cu<sub>2</sub>Co (h) and CsPbBr<sub>3</sub>@MOF-919-Cu<sub>2</sub>Zn (i).

(2.18 Å) was observed, confirming that Co disperses atomically in MOF-919-Cu<sub>2</sub>Co. It is worth noting that another scattering signal was present at 2.67 Å, which shows a slight shift compared with the Co-O-Co signal (2.58 Å) in CoO, thus can be assigned to the Co-O-Cu path [35,36]. The results of the best EXAFS fitting reveal that there are two Cu atoms around the second shell of Co (Fig. S5 and Table S4), which further supports the above conclusion that one of Cu in Cu<sub>3</sub> cluster was exchanged by one Co to form Cu<sub>2</sub>Co cluster at the soaking time of 24 h. Furthermore, the best fitting results of Co-N/O shell demonstrate that each Co is coordinated by four atoms, which can be assigned to two O and two N atoms (Table S4) [28]. Similar to MOF-919-Cu<sub>2</sub>Co, one of Cu in Cu<sub>3</sub> cluster was exchanged by one Zn to form Cu<sub>2</sub>Zn cluster in MOF-919-Cu<sub>2</sub>Zn at the soaking time of 24 h (Figs. 1a, c, S1, S2, S4 and S6, Tables S1 and S4).

Subsequently, the encapsulation of CsPbBr $_3$  QDs in the pores of MOF-919-Cu $_2$ M to form CsPbBr $_3$ @MOF-919-Cu $_2$ M composites was achieved by immersing the activated MOF-919-Cu $_2$ M in 0.01 M DMF solution of PbBr $_2$ , followed by immersing in methanol solution of CsBr [37]. Powder XRD patterns show that the skeleton of MOF-919-Cu $_2$ M are well kept after the encapsulation of CsPbBr $_3$  QDs (Fig. S7). Furthermore, no

powder XRD characteristic peak of CsPbBr3 was observed in CsPbBr<sub>3</sub>@MOF-919-Cu<sub>2</sub>M composites due to the small size of CsPbBr<sub>3</sub> (Fig. S7) [37]. The results of TEM images demonstrate that the CsPbBr<sub>3</sub> QDs are distributed uniformly in MOF-919-Cu<sub>2</sub>M with the similar size of about 3.8 nm (Figs. 1d-1f and S8). The HRTEM images show lattice fringes of about 0.31 nm (Fig. 1g-1i), which can be attributed to the (100) crystal face of CsPbBr<sub>3</sub> QDs [24]. EDS mappings disclose the homogeneous distribution of Cs, Pb, Br, Sc, Cu, Zn and Co elements in CsPbBr<sub>3</sub>@MOF-919-Cu<sub>2</sub>M composites (Figs. S9-S11). The N<sub>2</sub> adsorption isotherms of CsPbBr<sub>3</sub>@MOF-919-Cu<sub>2</sub>M composites demonstrate that the saturated N2 uptakes are sharply reduced compared with those of MOF-919-Cu<sub>2</sub>M, and the corresponding pore size distributions and BET surface area also display this trend (Figs. S1, S2, S12 and S13, Table S5). These results confirm that the CsPbBr3 QDs are successfully encapsulated in the pores of MOF-919-Cu<sub>2</sub>M [24,37]. Despite this, CsPbBr<sub>3</sub>@MOF-919-Cu<sub>2</sub>M still exhibit CO<sub>2</sub> adsorption performance, in which the CsPbBr<sub>3</sub>@MOF-919-Cu<sub>2</sub>Co displays the highest CO<sub>2</sub> uptake (Fig. S14). This may be attributed to the large BET surface area (Table S5). In addition, the results of ICP-MS analysis show that the ratios of Cs:Pb are about 1:1 and the amounts of CsPbBr3 QDs are about

4.4 wt% in CsPbBr<sub>3</sub>@MOF-919-Cu<sub>2</sub>M composites (Table S6). For comparison, the CsPbBr<sub>3</sub> QDs stabilized by OA and OM were also prepared (Fig. S7) [24].

To investigate the metal valence states of Cu<sub>2</sub>M clusters in MOF-919-Cu<sub>2</sub>M and CsPbBr<sub>3</sub>@MOF-919-Cu<sub>2</sub>M, as well as the interfacial interaction between MOF-919-Cu<sub>2</sub>M and CsPbBr<sub>3</sub> QDs in CsPbBr<sub>3</sub>@MOF-919-Cu<sub>2</sub>M, the XPS was carried out. As shown in Figs. S15 and S16, the Cu 2p XPS spectra of MOF-919-Cu<sub>2</sub>M and CsPbBr<sub>3</sub>@MOF-919-Cu<sub>2</sub>M show two kinds of Cu 2p<sub>3/2</sub> binding energies at about 932.8 and 934.8 eV, respectively, with the Auger peaks at about 570.8 eV, unveiling the mixed Cu<sup>+</sup>/Cu<sup>2+</sup> valence state of Cu species in these catalysts [28,38]. The XPS spectra of MOF-919-Cu<sub>2</sub>Co and CsPbBr<sub>3</sub>@MOF-919-Cu<sub>2</sub>Co display Co 2p3/2 and Co 2p1/2 characteristic peaks with two corresponding satellite peaks, demonstrating that the valence state of Co species is also + 2 (Fig. S17) [39]. For Zn atom in MOF-919-Cu<sub>2</sub>Zn and CsPbBr<sub>3</sub>@MOF-919-Cu<sub>2</sub>Zn, the binding energy difference between Zn  $2p_{3/2}$  and Zn  $2p_{1/2}$  is about 23.1 eV, revealing the valence state of Zn species is +2 in the two catalysts (Fig. S18) [40]. Additionally, the binding energies of Cu 2p, Co 3d and Zn 2p of CsPbBr<sub>3</sub>@MOF-919-Cu<sub>2</sub>M display negative shift compared with those in MOF-919-Cu<sub>2</sub>M (Figs. S15, S17 and S18), suggesting that MOF-919-Cu<sub>2</sub>M in CsPbBr<sub>3</sub>@MOF-919-Cu<sub>2</sub>M obtains electrons. The binding energies of Pb 4 f and Br 3d of CsPbBr<sub>3</sub>@MOF-919-Cu<sub>2</sub>M show positive shift compared with those in CsPbBr3 QDs, revealing that CsPbBr3 CsPbBr<sub>3</sub>@MOF-919-Cu<sub>2</sub>M loses electrons (Figs. S19 and S20). These results demonstrate that electron transfer happens from CsPbBr3 QDs to MOF-919-Cu<sub>2</sub>M in CsPbBr<sub>3</sub>@MOF-919-Cu<sub>2</sub>M.

The solid UV–vis absorption measurements of CsPbBr $_3$  QDs, MOF-919-Cu $_2$ M and CsPbBr $_3$ @MOF-919-Cu $_2$ M were performed to investigate their light absorbance ability. As shown in Fig. S21, the pristine CsPbBr $_3$  QDs displays strong light absorbance ability in both ultraviolet and visible light ranges. By contrast, the pristine MOF-919-Cu $_2$ M mainly absorbs ultraviolet and weak visible light (Figs. 2a, S22 and S23). After the encapsulation of CsPbBr $_3$  QDs in the pores of MOF-919-Cu $_2$ M, the

resulting CsPbBr<sub>3</sub>@MOF-919-Cu<sub>2</sub>M composites exhibit obviously improved light-harvesting ability compared with the pristine MOF-919-Cu<sub>2</sub>M (Figs. 2a, S22 and S23). The band-gap energies (Eg) of the pristine CsPbBr<sub>3</sub> QDs, MOF-919-Cu<sub>2</sub>, MOF-919-Cu<sub>2</sub>Co and MOF-919-Cu<sub>2</sub>Zn are 2.27, 2.67, 2.74 and 2.67 eV respectively, which are estimated by the Kubelka-Munk (KM) method based on their solid UV-vis absorption spectroscopy (Figs. S24-S27) [39]. Moreover, the lowest unoccupied molecular orbitals (LUMO) of the pristine CsPbBr<sub>3</sub> QDs, MOF-919-Cu<sub>3</sub>, MOF-919-Cu<sub>2</sub>Co and MOF-919-Cu<sub>2</sub>Zn are -1.03, -0.87, -0.76 and -0.78 V vs. normal hydrogen electrode (NHE), respectively, as determined by the results of Mott-Schottky measurements (Figs. 2b and S28-S30) [39]. Therefore, the highest occupied molecular orbitals (HOMO) of them are calculated to be 1.24, 1.80, 1.98 and 1.89 V vs. NHE, respectively (Figs. 2c, S31 and S32). Obviously, the LUMO of CsPbBr3 QDs and MOF-919-Cu2M are more negative compared with some photocatalytic products of CO<sub>2</sub> reduction such as CO (-0.53 V), HCOOH (-0.61 V) and CH<sub>4</sub> (-0.24 V). Furthermore, the HOMO of them are more positive than the oxidation potential of  $H_2O/O_2$  (0.81 V) [39]. All potentials are with reference to NHE with pH = 7. These results imply that the pristine CsPbBr<sub>3</sub> QDs and MOF-919-Cu<sub>2</sub>M are theoretically feasible for photocatalytic CO2 reduction and H2O oxidation. Additionally, we note that CsPbBr3 QDs and MOF-919-Cu2M show staggered band structures, suggesting the type-II or Z-scheme heterojunctions on CsPbBr<sub>3</sub>@MOF-919-Cu<sub>2</sub>M composites may be formed upon light irradiation (Figs. 2c, S31 and S32) [41,42].

To identify the type of CsPbBr<sub>3</sub>@MOF-919-Cu<sub>2</sub>M heterojunctions, the *in situ* XPS measurements in the dark and under the light irradiation were performed [43]. The results show that the binding energies of Cs 3d, Pb 4 f and Br 3d display positive shift upon light irradiation compared with those in the dark, suggesting that the CsPbBr<sub>3</sub> loses electrons (Figs. 2d, e and S33-S35). By contrast, the binding energies of Cu 2p (Cu<sup>2+</sup>) show negative shift upon light irradiation compared with those in the dark, hinting that MOF-919-Cu<sub>2</sub>M obtains electrons (Fig. 2 f, S36 and S37). Furthermore, the EPR measurements of CsPbBr<sub>3</sub> QDs,

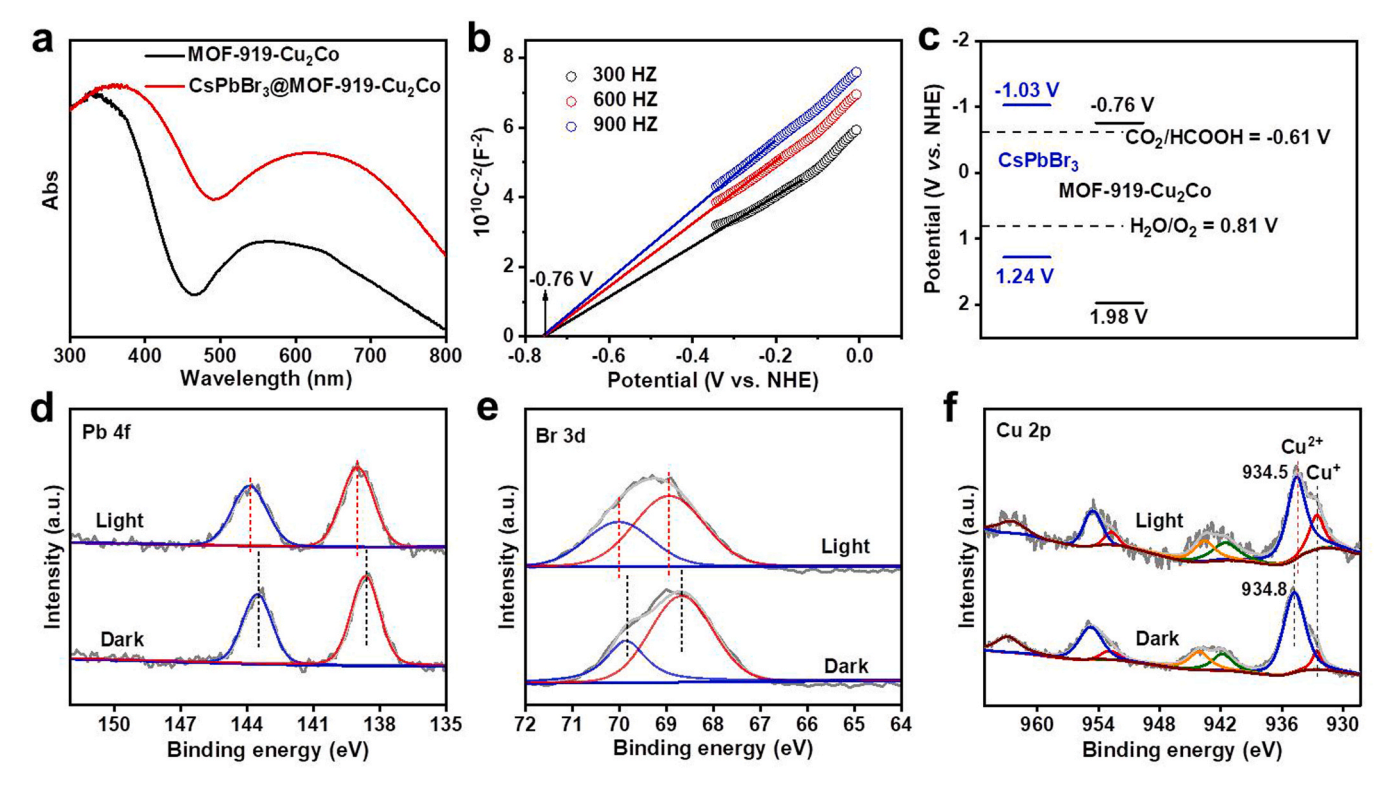


Fig. 2. (a) UV–vis spectra of the pristine MOF-919- $Cu_2Co$  and CsPbBr<sub>3</sub>@MOF-919- $Cu_2Co$ . (b) Mott–Schottky plots of MOF-919- $Cu_2Co$ . (c) Band-structure diagram for the pristine CsPbBr<sub>3</sub> and MOF-919- $Cu_2Co$  before contact. (d-f) XPS spectra for Pb 4 f (d), Br 3d (e) and Cu 2p (f) of CsPbBr<sub>3</sub>@MOF-919- $Cu_2Co$  in the dark and upon light irradiation.

MOF-919-Cu<sub>2</sub>Co and CsPbBr<sub>3</sub>@MOF-919-Cu<sub>2</sub>Co with 5,5-dimethyl-1-pyrroline-N-oxide (DMPO) as probes were performed to monitor the generation of  $\cdot O_2^-$  and  $\cdot OH$  species. As shown in Fig. S38, the characteristic signals of DMPO-O2 for the pristine CsPbBr3 QDs and MOF-919-Cu<sub>2</sub>Co, as well as CsPbBr<sub>3</sub>@MOF-919-Cu<sub>2</sub>Co were detected under light irradiation, in which CsPbBr<sub>3</sub>@MOF-919-Cu<sub>2</sub>Co exhibits stronger signals than the pristine CsPbBr<sub>3</sub> QDs and MOF-919-Cu<sub>2</sub>Co. These results suggest that MOF-919-Cu<sub>2</sub>Co of CsPbBr<sub>3</sub>@MOF-919--Cu<sub>2</sub>Co possesses more photogenerated electrons than the pristine MOF-919-Cu<sub>2</sub>Co, indicating the occurrence of electron transfer from CsPbBr<sub>3</sub> QDs to MOF-919-Cu<sub>2</sub>Co. Moreover, the weak characteristic signals of DMPO $-\cdot$ OH for the pristine MOF-919-Cu<sub>2</sub>Co were observed under light irradiation, while no characteristic DMPO--OH signal was observed for CsPbBr<sub>3</sub>@MOF-919-Cu<sub>2</sub>Co. This result hints that the pristine MOF-919-Cu<sub>2</sub>Co has more photogenerated holes than MOF-919--Cu<sub>2</sub>Co of CsPbBr<sub>3</sub>@MOF-919-Cu<sub>2</sub>Co, demonstrating that the hole transfer occurs from MOF-919-Cu<sub>2</sub>Co to CsPbBr<sub>3</sub> CsPbBr<sub>3</sub>@MOF-919-Cu<sub>2</sub>Co. These results demonstrate that the type-II heterojunctions between CsPbBr3 QDs and MOF-919-Cu2M were formed in CsPbBr<sub>3</sub>@MOF-919-Cu<sub>2</sub>M composites, which might facilitate charge separation and transfer efficiencies in photocatalytic CO<sub>2</sub> reduction compared with the pristine CsPbBr<sub>3</sub> QDs and MOF-919-Cu<sub>2</sub>M. For comparison, the type-II heterojunctions of CsPbBr<sub>3</sub>/MOF-919-Cu<sub>2</sub>M were also fabricated by physical mixture of CsPbBr3 QDs and

MOF-919-Cu<sub>2</sub>M (Figs. S39-S44).

## 3.2. Photocatalytic CO<sub>2</sub> reduction experiments

Encouraged by the above analysis, the photocatalytic CO2 reduction experiments of CsPbBr<sub>3</sub> QDs, MOF-919-Cu<sub>2</sub>M, CsPbBr<sub>3</sub>/MOF-919-Cu<sub>2</sub>M and CsPbBr<sub>3</sub>@MOF-919-Cu<sub>2</sub>M were performed in CO<sub>2</sub>-saturated acetonitrile solution with small amount of H<sub>2</sub>O under visible-light irradiation, in absence of additional photosensitizers and sacrificial agents. The results demonstrate that MOF-919-Cu<sub>2</sub>M, CsPbBr<sub>3</sub>/MOF-919-Cu<sub>2</sub>M and CsPbBr<sub>3</sub>@MOF-919-Cu<sub>2</sub>M can reduce CO<sub>2</sub> to HCOOH (Fig. S45) [16], while the pristine CsPbBr3 QDs can reduce CO2 to CO. Firstly, the relationship between catalytic activity and the content of Co was investigated for CsPbBr<sub>3</sub>@MOF-919-Cu<sub>x</sub>Co<sub>y</sub>. As shown in Fig. S46 and Table S1, the HCOOH production rate was linearly increased along with the increase of Co content, and reached a maximum value at the Cu:Co atomic ratio of 2:1. Further increasing the Co content caused the decrease of HCOOH production rate. Secondly, the relationship between catalytic activity and the amount of CsPbBr3 QDs encapsulated in the pores of MOF-919-Cu<sub>2</sub>Co was also investigated. CsPbBr<sub>3</sub>@MOF-919--Cu<sub>2</sub>Co exhibits the enhanced HCOOH generation rate along with the increased amount of CsPbBr3 QDs when it is less than 4.4 %. However, the HCOOH production rate drops with further incremental CsPbBr<sub>3</sub> QDs, which may be attributed to the obstacles of mass transfer for CO2

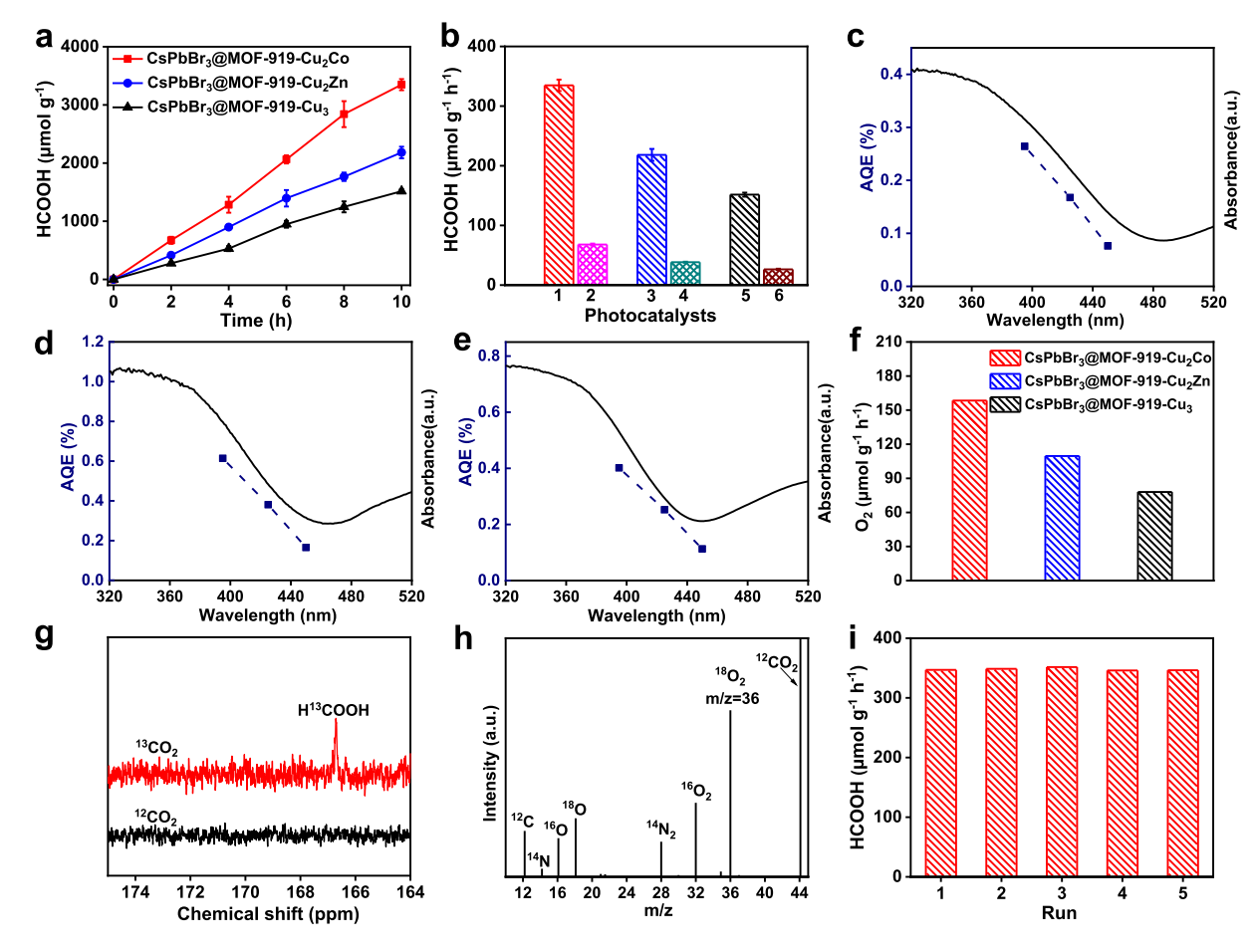


Fig. 3. (a) Time-dependent HCOOH generation of photocatalytic  $CO_2$  reduction over  $CsPbBr_3@MOF-919-Cu_2M$ . (b) HCOOH production rates of  $CsPbBr_3@MOF-919-Cu_2M$  and  $CsPbBr_3/MOF-919-Cu_2M$  (1:  $CsPbBr_3@MOF-919-Cu_2Co$ ; 2:  $CsPbBr_3/MOF-919-Cu_2Co$ ; 3:  $CsPbBr_3@MOF-919-Cu_2Zn$ ; 4:  $CsPbBr_3/MOF-919-Cu_2Zn$ ; 5:  $CsPbBr_3@MOF-919-Cu_3$ ; 6:  $CsPbBr_3/MOF-919-Cu_3$ . (c-e) UV-vis absorption spectra and AQE values of  $CsPbBr_3@MOF-919-Cu_3$  (c),  $CsPbBr_3@MOF-919-Cu_2Zn$  (d) and  $CsPbBr_3@MOF-919-Cu_2Co$  (e). (f)  $The O_2$  production rates of  $CsPbBr_3@MOF-919-Cu_3$ ,  $CsPbBr_3@MOF-919-Cu_2Zn$  and  $CsPbBr_3@MOF-919-Cu_2Co$ . (g) Toughtarrow T

photoreduction due to too many CsPbBr<sub>3</sub> QDs encapsulated in the pores of MOF-919-Cu<sub>2</sub>Co (Fig. S47 and Table S7). Therefore, the photocatalytic activities of CsPbBr<sub>3</sub>@MOF-919-Cu<sub>2</sub>Co show volcano-type trends on the whole, and CsPbBr<sub>3</sub>@MOF-919-Cu<sub>2</sub>Co presents the highest HCOOH generation rate of 334.8 µmol g<sup>-1</sup> h<sup>-1</sup> at the Cu:Co atomic ratio of 2:1 and CsPbBr<sub>3</sub> QDs amount of about 4.4 % (Figs. 3a and 3b). Moreover, the HCOOH generation rates of CsPbBr<sub>3</sub>@MOF-919-Cu<sub>3</sub> and CsPbBr<sub>3</sub>@MOF-919-Cu<sub>2</sub>Zn are 151.6 and 218.2 µmol g<sup>-1</sup> h<sup>-1</sup>, respectively (Fig. 3a and b). In sharp contrast, the pristine CsPbBr3 QDs, MOF-919-Cu<sub>2</sub>Xn and MOF-919-Cu<sub>2</sub>Co display significantly decreased CO and HCOOH production rates of 5.2, 6.0, 12.4 and 15.9  $\mu$ mol g<sup>-1</sup> h<sup>-1</sup>, respectively (Figs. 3a, b and S48). Obviously, CsPbBr<sub>3</sub>@MOF-919-Cu<sub>2</sub>Co achieves the highest photocatalytic activity with the electron consumption rate ( $R_{\text{electron}}$ ) of 669.6  $\mu$ mol g<sup>-1</sup> h<sup>-1</sup> for HCOOH production, which is 64 and 56 times higher than those of the pristine CsPbBr<sub>3</sub> QDs and MOF-919-Cu<sub>3</sub>, respectively. Moreover, the photocatalytic performance of CsPbBr<sub>3</sub>@MOF-919-Cu<sub>2</sub>M are much higher than those of CsPbBr<sub>3</sub>/MOF-919-Cu<sub>2</sub>M (Fig. 3b), suggesting that the encapsulation of CsPbBr<sub>3</sub> QDs in the pores of MOF-919-Cu<sub>2</sub>M could accelerate charge transfer efficiency. It's also worth noting that the catalytic activity of CsPbBr<sub>3</sub>@MOF-919-Cu<sub>2</sub>Co is superior to most of the reported MOF/COF-based photocatalysts for artificial photosynthesis (Table S8). Furthermore, the AQE of CsPbBr<sub>3</sub>@MOF-919-Cu<sub>2</sub>M was measured at 395, 425 and 450 nm [44]. As shown in Fig. 3c-e, they exhibit different AQEs at the tested wavelengths, following the sequence CsPbBr<sub>3</sub>@MOF-919-Cu<sub>2</sub>Co > CsPbBr<sub>3</sub>@MOF-919-Cu<sub>2</sub>Zn > CsPbBr<sub>3</sub>@MOF-919-Cu<sub>3</sub>, which the AOE

CsPbBr $_3$ @MOF-919-Cu $_2$ Co was 0.38 % under 425 nm. These results also demonstrate that the CO $_2$  photoreduction activity can be boosted simply via regulating the dual-metal sites in Cu $_2$ M cluster-based MOFs. Moreover, O $_2$  was detected in the catalytic system, with O $_2$  generation rates of 77.0, 109.6 and 158.4 µmol g $^{-1}$  h $^{-1}$  for CsPbBr $_3$ @MOF-919-Cu $_3$ , CsPbBr $_3$ @MOF-919-Cu $_2$ Zn and CsPbBr $_3$ @MOF-919-Cu $_2$ Co, respectively (Fig. 3f). The stoichiometric ratios of HCOOH and O $_2$  for CsPbBr $_3$ @MOF-919-Cu $_2$ M are all close to 2:1. In addition, no other reduction product such as CO, CH $_4$ , CH $_3$ OH, C $_2$ H $_4$ , C $_2$ H $_5$ OH and H $_2$  was detected, suggesting the electrons generated through H $_2$ O oxidation are all used to the reduction of CO $_2$  to HCOOH and the HCOOH selectivities are nearly 100 %.

To confirm the sources of HCOOH and  $O_2$ , a series of control experiments over CsPbBr<sub>3</sub>@MOF-919-Cu<sub>2</sub>Co were carried out. The results show that no HCOOH was detected without catalyst,  $CO_2$ ,  $H_2O$  or light irradiation, indicating that these factors are all indispensable and  $H_2O$  is the electron source for  $CO_2$  photoreduction to HCOOH. Moreover,  $^{13}CO_2$  and  $H_2^{18}O$  isotope trace experiments were further performed. As shown in Fig. 3g, the  $^{13}C$  NMR spectrum displays an obvious signal at 166.7 ppm, which can be attributed to the  $H^{13}COOH$ , unambiguously confirming that the carbon source of HCOOH indeed originates from  $CO_2$  reduction [39]. The result of MS shows a peak at m/z = 36, corresponding to  $^{18}O_2$  (Fig. 3h), verifying that the electron source of  $CO_2$  photoreduction comes from water oxidation [24]. The photocatalytic durability of CsPbBr<sub>3</sub>@MOF-919-Cu<sub>2</sub>Co was evaluated by consecutive recycling experiments. The HCOOH production rates can be well retained during the five consecutive cycles (Fig. 3i). Additionally, the

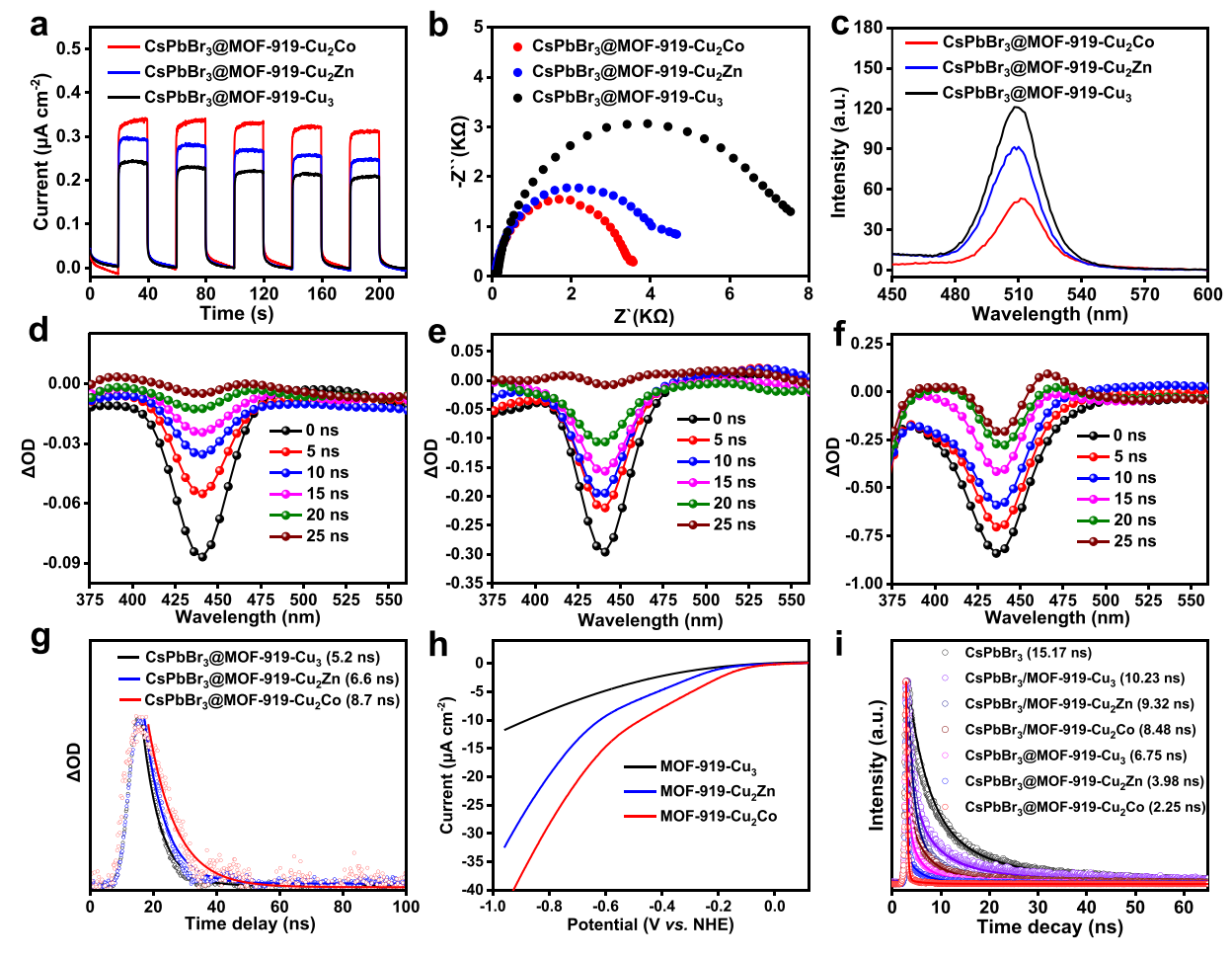


Fig. 4. (a) Photocurrent responses, (b) EIS plots and (c) PL spectra of CsPbBr<sub>3</sub>@MOF-919-Cu<sub>2</sub>M. (d-f) TA spectra at different delay times for CsPbBr<sub>3</sub>@MOF-919-Cu<sub>3</sub>(d), CsPbBr<sub>3</sub>@MOF-919-Cu<sub>2</sub>D. (e) and CsPbBr<sub>3</sub>@MOF-919-Cu<sub>2</sub>D. (f). (g) TA kinetic traces of CsPbBr<sub>3</sub>@MOF-919-Cu<sub>2</sub>M at 440 nm. (h) The LSV profiles for MOF-919-Cu<sub>2</sub>M. (i) Time-resolved PL spectra of CsPbBr<sub>3</sub> QDs, CsPbBr<sub>3</sub>/MOF-919-Cu<sub>2</sub>M and CsPbBr<sub>3</sub>@MOF-919-Cu<sub>2</sub>M.

results of powder XRD patterns show no loss of crystallinity for  $CsPbBr_3@MOF-919-Cu_2M$  after photocatalysis (Figs. S49-S51). The TEM images of  $CsPbBr_3@MOF-919-Cu_2M$  demonstrate that the sizes of  $CsPbBr_3$  QDs are hardly changed after photocatalysis (Figs. S52-S54). These results demonstrate that  $CsPbBr_3@MOF-919-Cu_2M$  possesses good stability in artificial photosynthesis.

The photocurrent response, EIS and PL emission spectra of CsPbBr<sub>3</sub> ODs, MOF-919-Cu<sub>2</sub>M, CsPbBr<sub>3</sub>/MOF-919-Cu<sub>2</sub>M and CsPbBr<sub>3</sub>@MOF-919-Cu<sub>2</sub>M were tested to study charge separation and transfer efficiencies, as well as to illustrate the different photocatalytic performance [45]. As shown in Figs. 4a and S55, all catalysts exhibit obvious photocurrent signals, among which the CsPbBr<sub>3</sub>@MOF-919-Cu<sub>2</sub>Co possesses the strongest response intensity, indicating the best separation of photo-generated electrons and holes. The results of EIS spectra reveal that CsPbBr<sub>3</sub>@MOF-919-Cu<sub>2</sub>Co shows the smallest semicircle radius. suggesting the fastest electron transfer (Figs. 4b and S56). Moreover, the PL spectra demonstrate that CsPbBr<sub>3</sub>@MOF-919-Cu<sub>2</sub>Co displays the weakest emission intensity, also disclosing the most efficient charge separation (Figs. 4c and S57). In addition, the TA spectra of CsPbBr<sub>3</sub>@MOF-919-Cu<sub>2</sub>M were carried out to investigate charge-separated state [46,47]. As shown in Fig. 4d-g, the strong bleaching signals around 440 nm were observed upon pulsed laser excitation, and the lifetimes of the charge-separated state were found to 5.2, and 8.7 ns for CsPbBr<sub>3</sub>@MOF-919-Cu<sub>3</sub>, CsPbBr<sub>3</sub>@MOF-919-Cu<sub>2</sub>Zn and CsPbBr<sub>3</sub>@MOF-919-Cu<sub>2</sub>Co, respectively. These results certify again that CsPbBr<sub>3</sub>@MOF-919-Cu<sub>2</sub>Co shows the most efficient charge separation. Besides, the LSV measurements of MOF-919-Cu<sub>2</sub>M were performed in CO<sub>2</sub> atmosphere to study the thermodynamics of CO<sub>2</sub> reduction [14]. It is apparent that the onset overpotential of MOF-919-Cu<sub>2</sub>Co is the lowest (Fig. 4h), suggesting that MOF-919-Cu<sub>2</sub>Co is thermodynamically superior to MOF-919-Cu<sub>3</sub> and MOF-919-Cu<sub>2</sub>Zn for CO<sub>2</sub> reduction. The ECSA of MOF-919-Cu<sub>2</sub>M and CsPbBr<sub>3</sub>@MOF-919-Cu<sub>2</sub>M were also performed. As shown in Figs. S58 and S59, CsPbBr<sub>3</sub>@MOF-919-Cu<sub>2</sub>Co displays the largest ECSA, implying its highest photocatalytic activity. All the results above unambiguously explain the highest catalytic performance of CsPbBr<sub>3</sub>@MOF-919-Cu<sub>2</sub>Co for CO<sub>2</sub> photoreduction to HCOOH.

To further illustrate the much higher photocatalytic performance of  $CsPbBr_3@MOF-919-Cu_2M$  than those of  $CsPbBr_3/MOF-919-Cu_2M$ , the electron transfer rates between  $CsPbBr_3$  QDs and  $MOF-919-Cu_2M$  were evaluated. The TRPL spectra of  $CsPbBr_3$  QDs,  $CsPbBr_3/MOF-919-Cu_2M$  and  $CsPbBr_3@MOF-919-Cu_2M$  under excitation at 450 nm were carried out to calculate the electron transfer rate constant  $(k_{et})$  by the below expression [48]:

$$k_{\text{et}} = \frac{1}{\tau_{\text{(heterojuntion)}}} - \frac{1}{\tau_{\text{(CsPbBr}_3)}}$$

Here,  $\tau$  is the average lifetime. As shown in Fig. 4i, the  $\tau$  values of CsPbBr<sub>3</sub>/MOF-919-Cu<sub>3</sub>, CsPbBr<sub>3</sub>@MOF-919-Cu<sub>3</sub>, CsPbBr<sub>3</sub>/MOF-919-Cu<sub>2</sub>Zn, CsPbBr<sub>3</sub>@MOF-919-Cu<sub>2</sub>Zn, CsPbBr<sub>3</sub>/MOF-919-Cu<sub>2</sub>Co and CsPbBr<sub>3</sub>@MOF-919-Cu<sub>2</sub>Co are 10.23, 6.75, 9.32, 3.98, 8.48 and 2.25 ns respectively, corresponding to the  $k_{\rm et}$  values of  $3.18 \times 10^7$ ,  $8.21 \times 10^7$ ,  $4.13 \times 10^7$ ,  $1.85 \times 10^8$ ,  $5.19 \times 10^7$  and  $3.78 \times 10^8$  s<sup>-1</sup>, respectively. Obviously, CsPbBr<sub>3</sub>@MOF-919-Cu<sub>2</sub>M exhibit larger k<sub>et</sub> values than those of CsPbBr<sub>3</sub>/MOF-919-Cu<sub>2</sub>M, revealing the faster electron transfer from CsPbBr3 QDs to MOF-919-Cu2M. These results demonstrate that the CsPbBr<sub>3</sub>@MOF-919-Cu<sub>2</sub>M exhibits more efficient charge separation and transfer than CsPbBr<sub>3</sub>/MOF-919-Cu<sub>2</sub>M. Additionally, DFT calculations were carried out to further study the charge transfer between CsPbBr3 QDs and MOF-919-Cu2M. Taking CsPbBr3@MOF-919-Cu2Co for an example, when the CsPbBr3 QDs were close to the MOF-919-Cu<sub>2</sub>Co, the charge transfer between them was more efficient (Fig. S60) [37]. All the above results unambiguously show that the encapsulation of CsPbBr3 QDs in the pores of MOF-919-Cu2M greatly facilitates the charge transfer efficiency, thus significantly improving the catalytic activity for CO2 photoreduction.

#### 3.3. Photocatalytic mechanism

The possible mechanism for CO<sub>2</sub> photoreduction coupled with H<sub>2</sub>O oxidation over CsPbBr3@MOF-919-Cu2M was elucidated by in situ EPR measurement. The results demonstrate that CsPbBr<sub>3</sub>@MOF-919-Cu<sub>3</sub> shows a strong  $Cu^{2+}$  signal at g = 2.10 in the dark (Fig. 5a), which is obviously decreased upon light irradiation, suggesting that Cu<sup>2+</sup> was reduced to Cu<sup>+</sup> [49,50]. CsPbBr<sub>3</sub>@MOF-919-Cu<sub>2</sub>Zn also exhibits a strong signal at g=2.10 in the dark, which can be assigned to  $Cu^{2+}$ because the Zn<sup>2+</sup> do not generate EPR signal. This signal shows an evident decrease upon light irradiation, hinting that Cu<sup>2+</sup> is transformed to Cu<sup>+</sup> (Fig. S61) [49,50]. For CsPbBr<sub>3</sub>@MOF-919-Cu<sub>2</sub>Co, a strong EPR signal can be observed at g = 2.13 in the dark, which can be assigned to the combined signals of  $Cu^{2+}$  and  $Co^{2+}$  [49–51]. Upon light irradiation, this signal shows a slight decrease, which may be attributed to the reduction of only Cu<sup>2+</sup> to Cu<sup>+</sup>, owing to its insufficient conduction band potential (-0.76 V vs. NHE) for the reduction of  $Co^{2+}$  to  $Co^{+}$  (-1.10 V vs. NHE) (Fig. 5b and f) [49-51]. These results suggest that MOF-919-Cu<sub>2</sub>M obtains electrons upon visible light irradiation, which are agree well with the results of in situ XPS (Fig. 2f, S36 and S37). Considering the type-II heterojunction of CsPbBr<sub>3</sub>@MOF-919-Cu<sub>2</sub>M, the reaction pathways were proposed. Upon light irradiation, both CsPbBr3 QDs and MOF-919-Cu<sub>2</sub>M absorb light to generate electrons and holes. The photogenerated holes in the HOMO of MOF-919-Cu<sub>2</sub>M are transferred to the HOMO of CsPbBr<sub>3</sub> QDs to oxidize H<sub>2</sub>O to O<sub>2</sub> (Fig. S62). The O<sub>2</sub> formation at the CsPbBr3 QDs has been previously identified as a water nucleophilic attack (WNA) mechanism with the following steps [52]: 1) H<sub>2</sub>O + \*  $\rightarrow$  \*OH + H<sup>+</sup> + e<sup>-</sup>; 2) \*OH  $\rightarrow$  \*O + H<sup>+</sup> + e<sup>-</sup>; 3) H<sub>2</sub>O + \*O  $\rightarrow$  \*OOH  $+ H^+ + e^-$ ; 4) \*OOH  $\rightarrow$  O<sub>2</sub>  $+ H^+ + e^- + *$  (\* stands for an active site). Moreover, the photogenerated electrons in the LUMO of CsPbBr3 QDs are transferred to the LUMO of MOF-919-Cu<sub>2</sub>M to reduce CO<sub>2</sub> to HCOOH (Fig. S62).

To see if the HCOOH generated by MOF-919-Cu<sub>2</sub>M will be oxidized by CsPbBr3 QDs in the catalytic process. The photocatalytic experiment over CsPbBr<sub>3</sub>@MOF-919-Cu<sub>2</sub>Co was performed under the N<sub>2</sub> atmosphere in the presence of H<sup>13</sup>COOH (0.2 µL). As shown in Fig. S63, negligible <sup>13</sup>CO<sub>2</sub> peak was detected by the mass spectrum, suggesting that no H13COOH was oxidized by CsPbBr3 QDs, which may be attributed to the much lower concentration of  $H^{13}COOH$  than  $H_2O$  (20  $\mu L$ ) in the photocatalytic system. Moreover, the influence of O2 generated by CsPbBr<sub>3</sub> QDs to CO<sub>2</sub> photoreduction on Cu<sub>2</sub>M sites was also investigated. Taking CsPbBr<sub>3</sub>@MOF-919-Cu<sub>2</sub>Co as an example, the reaction solution withDMPO as the trapping agent after the CO<sub>2</sub> photoreduction was collected for the EPR measurement [53]. The characteristic signals of DMPO-O<sub>2</sub> were almost negligible, suggesting that the generated O<sub>2</sub> was hardly reduced (Fig. S64), which may be attributed to the much higher CO<sub>2</sub> concentration around Cu<sub>2</sub>M clusters than that of O<sub>2</sub>. These results demonstrate that the retarding effects of HCOOH on H2O oxidation and O2 on CO2 photoreduction can be avoided, which guaranteed the proceeding of artificial photosynthesis [53]. To detect the key intermediates in the process of CO2 photoreduction, in situ FTIR measurements of CsPbBr<sub>3</sub>@MOF-919-Cu<sub>2</sub>M were carried out. The results show that the new infrared absorption peaks at 1633, 1640 and  $1639\ cm^{-1}$ were detected for CsPbBr<sub>3</sub>@MOF-919-Cu<sub>3</sub>,  $CsPbBr_3@MOF-919-Cu_2Zn\ and\ CsPbBr_3@MOF-919-Cu_2Co\ respectively$ (Figs. 5c, S65 and S66), which can be assigned to the key intermediates of HCOO\* for HCOOH generation [54]. The intensities of these peaks gradually increase along with the incremental irradiation time, demonstrating the increased concentration of HCOO\* intermediates during the CO<sub>2</sub> photoreduction.

DFT calculation was further performed to elucidate how the  $CO_2$  photoreduction activity being regulated by the dual-metal sites, and the origin of the outstanding photocatalytic performance of  $CsPbBr_3@MOF-919-Cu_2Co$ . The primitive part of MOF-919- $Cu_2M$  were picked out for model building as the  $CO_2$  photoreduction was occurred at MOFs only [37,55]. The photocatalytic  $CO_2$  reduction to HCOOH involves a

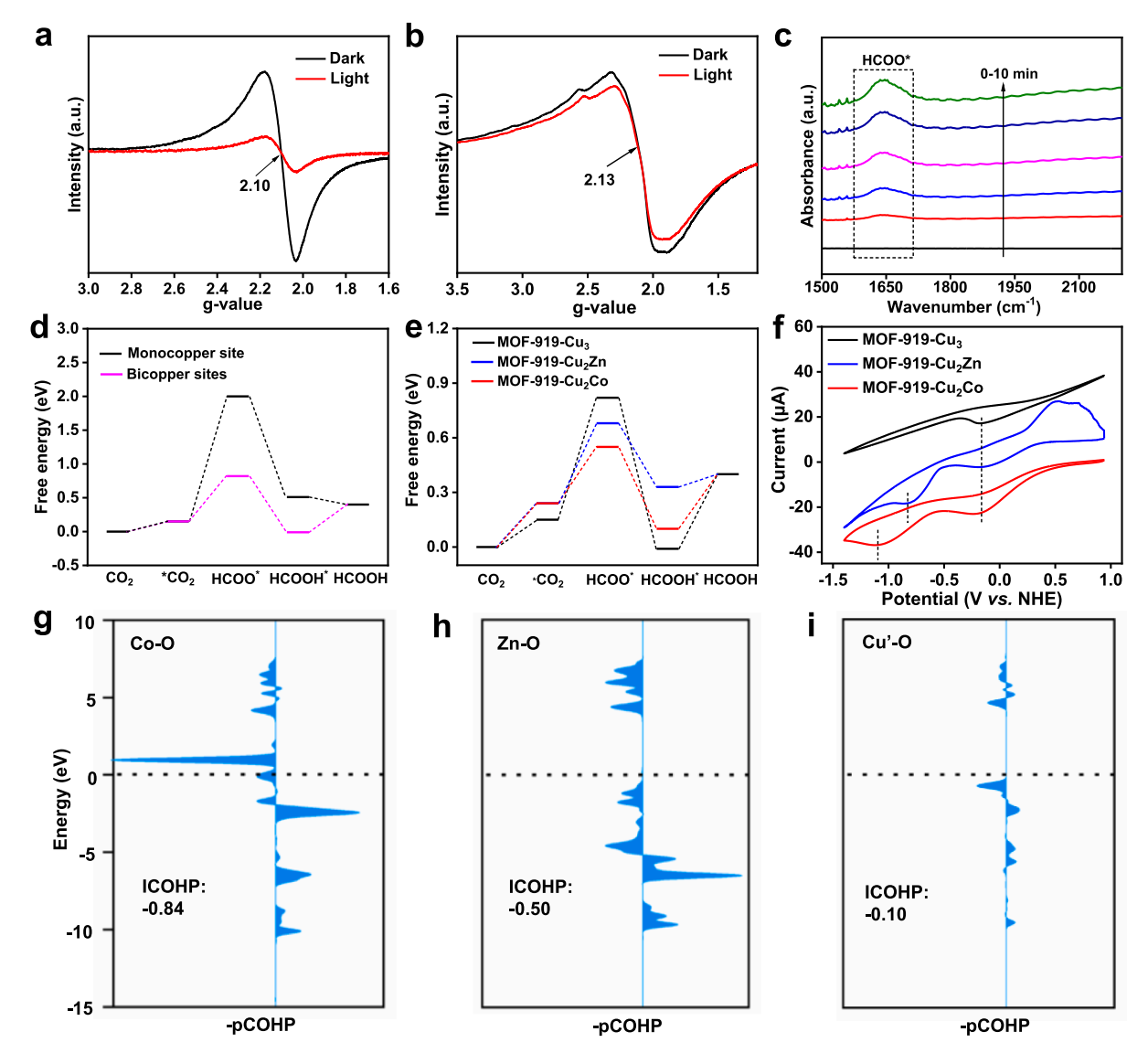


Fig. 5. EPR spectra of CsPbBr<sub>3</sub>@MOF-919-Cu<sub>3</sub> (a) and CsPbBr<sub>3</sub>@MOF-919-Cu<sub>2</sub>Co (b) in the dark and light irradiation. (c) *In situ* FTIR spectra of CsPbBr<sub>3</sub>@MOF-919-Cu<sub>2</sub>Co in the process of photocatalytic CO<sub>2</sub> reduction. (d) Free energy profiles for the photoreduction of CO<sub>2</sub> to HCOOH for MOF-919-Cu<sub>3</sub> with monocopper and bicopper sites. (e) Free energy profiles for the photoreduction of CO<sub>2</sub> to HCOOH by MOF-919-Cu<sub>2</sub>M. (f) CV curves of MOF-919-Cu<sub>2</sub>M. (g-i) The COHP analysis between Co/Zn/Cu' and adjacent O atom of HCOO\* intermediate for MOF-919-Cu<sub>2</sub>Co (g), MOF-919-Cu<sub>2</sub>Zn (h) and MOF-919-Cu<sub>3</sub> (i).

two-electron and two-proton transfer process [56]. First, CO<sub>2</sub> is adsorbed at the catalytic site and receive an electron and a proton to form HCOO\*. Subsequently, the hydrogenation of HCOO\* happens on one O atom to form HCOOH\*. Finally, HCOOH desorption occurs. To see if the dimetallic centers is beneficial for CO<sub>2</sub> photoreduction, taking MOF-919-Cu<sub>3</sub> as an example, the free-energy change (ΔG) of CO<sub>2</sub> photoreduction on monocopper and bicopper sites were calculated, respectively (Fig. S67). As shown in Fig. 5d, the  $\Delta G$  values of the rate-determining step (RDS) for the formation of HCOO\* are 1.85 and 0.67 eV for monocopper and bicopper sites respectively, suggesting the photocatalytic CO2 reduction by MOF-919-Cu3 prefers to follow a dual-metal synergistic catalysis process. After the exchange of one Cu with one Zn or Co, the  $\Delta G$  values of RDS decrease from 0.67 eV for MOF-919-Cu $_3$  to 0.44 for MOF-919-Cu $_2$ Zn and 0.31 eV for MOF-919--Cu<sub>2</sub>Co respectively, suggesting the strengthened synergistic catalysis effect between Cu and Zn/Co (Figs. 5e, S68 and S69a). In addition, we calculated the  $\Delta G$  of  $CO_2$  photoreduction for MOF-919-CuCo<sub>2</sub> with CuCo<sub>2</sub> cluster (Fig. S69b). The RDS for MOF-919-CuCo<sub>2</sub> is the desorption of HCOOH\* with  $\Delta G$  value of 0.48 eV, which is larger than that of MOF-919-Cu<sub>2</sub>Co (Fig. S70). These results explain the highest catalytic

activity of CsPbBr<sub>3</sub>@MOF-919-Cu<sub>2</sub>Co among the all tested catalysts.

To understand why MOF-919-Cu<sub>2</sub>Co displays the lowest ΔG value of 0.31 eV for photocatalytic CO<sub>2</sub> reduction, the CV of MOF-919-Cu<sub>2</sub>M was firstly measured in Ar atmosphere. As shown in Fig. 5f, the CV of MOF-919-Cu<sub>3</sub> shows a reduction wave at -0.19 V vs. NHE, which is assigned to the reduction of Cu<sup>2+</sup> to Cu<sup>+</sup> [57–59]. By contrast, the CV of MOF-919-Cu<sub>2</sub>Zn displays two reduction waves at -0.16 and -0.82 V vs. NHE, corresponding to the reduction of Cu<sup>2+</sup> to Cu<sup>+</sup> and Zn<sup>2+</sup> to Zn, respectively [57-59]. Moreover, the CV of MOF-919-Cu<sub>2</sub>Co also shows two reduction waves at -0.21 and -1.10 V vs. NHE, which are assigned to the reduction of Cu<sup>2+</sup> to Cu<sup>+</sup> and Co<sup>2+</sup> to Co<sup>+</sup>, respectively [57–59]. Obviously,  $Co^{2+}/Co^{+}$  exhibits the lowest reduction potential and  $Co^{2+}$ cannot be reduced by the photo-induced electron with a reduction potential of only -0.76 V (Fig. 2c), thus cobalt keeps  $Co^{2+}$  valence state in the process of CO<sub>2</sub> photoreduction. The CV results are further supported by in situ XPS. As shown in Fig. 2f, S36 and S37, the binding energies of Cu 2p (Cu<sup>2+</sup>) display obviously negative shift and the molar ratios of Cu<sup>2+</sup>:Cu<sup>+</sup> decrease in CsPbBr<sub>3</sub>@MOF-919-Cu<sub>2</sub>M upon light irradiation compared with those in the dark, suggesting that part of Cu<sup>2+</sup> were reduced to Cu<sup>+</sup>. However, the binding energies of Zn 2p only show

slightly negative shift under the light irradiation, and Co 2p spectra are identical in the dark and light irradiation (Figs. S71 and S72), indicating only small amount of  $Zn^{2+}$  was reduced, and Co keeps + 2 valence state during the photocatalytic CO2 reduction process. Therefore, we can conclude that the interaction between Cu/Co and HCOO\* intermediate is stronger than Cu/Zn and Cu/Cu, as the high-valence state metals usually show stronger interaction to O than low-valence state metals [60]. Moreover, the crystal orbital Hamilton population (COHP) analysis was conducted to further evaluate the binding strengths between dual-metal sites and HCOO\* [61]. The integrated COHP (ICOHP) was obtained by integration of COHP over all levels up to the Fermi level, which can evaluate the binding strength (the more negative value of ICOHP, the stronger binding strength). As shown in Figs. 5g-5i, the values of ICOHP for Co-O, Zn-O and Cu'-O in MOF-919-Cu<sub>2</sub>Co, MOF-919-Cu<sub>2</sub>Zn and MOF-919-Cu<sub>3</sub> are -0.84, -0.50 and -0.10 eV, respectively (Cu'-O represents the Cu site in Cu<sub>3</sub> cluster corresponding to Zn and Co sites in Cu<sub>2</sub>Zn and Cu<sub>2</sub>Co clusters, respectively, see Fig. S67a). However, the values of ICOHP for Cu-O in the three samples are similar (Fig. S73). These results demonstrate that the binding strengths between Cu/Co and HCOO\* is the strongest, which agrees well with the results of CV, XPS and DFT calculation. All the above results solidly verify that the dual-metal synergistic effect between Cu and Co is stronger than those of Cu/Zn and Cu/Cu, which promote CO2 photoreduction to generate the best photocatalytic CO<sub>2</sub> reduction performance.

#### 4. Conclusion

In summary, by encapsulating CsPbBr3 QDs into the pores of dualmetal sites MOFs, three CsPbBr<sub>3</sub>@MOF-919-Cu<sub>2</sub>M composite catalysts were successfully constructed, which exhibit outstanding catalytic activities for CO2 photoreduction to HCOOH coupled with H2O oxidation to O2. Among which, CsPbBr3@MOF-919-Cu2Co shows the highest photocatalytic performance with a HCOOH production rate of 334.8 μmol g<sup>-1</sup> h<sup>-1</sup>, 64-, 56- and 5-fold higher than those of pristine CsPbBr<sub>3</sub> QDs, MOF-919-Cu<sub>3</sub>, and CsPbBr<sub>3</sub>/MOF-919-Cu<sub>2</sub>Co, respectively. Experimental and DFT calculation results reveal that the significantly enhanced photocatalytic activity of CsPbBr<sub>3</sub>@MOF-919-Cu<sub>2</sub>Co is not only attributed to the efficient charge separation due to the close contact of CsPbBr3 QDs and MOF-919-Cu2Co, but also due to the strengthened dual-metal synergistic catalysis effect between Cu and Co for dramatically lowering the RDS  $\Delta G$  value. This work demonstrates that the photocatalytic performance of CO<sub>2</sub> reduction can be significantly promoted by combining efficient charge separation and dual-metalsynergistic catalysis.

## CRediT authorship contribution statement

Di-Chang Zhong: Writing – original draft, Conceptualization. Tong-Bu Lu: Supervision, Funding acquisition. Hong-Juan Wang: Software. Jing-Jing Wang: Data curation. Jing-Yi Liu: Methodology. Yun-Nan Gong: Writing – review & editing, Supervision, Investigation, Conceptualization. Hao-Yu Yang: Data curation. Chong-Jiu Lu: Investigation.

## **Declaration of Competing Interest**

The authors declare no competing financial interest.

## Acknowledgements

This work was supported by National Key R&D Program of China (2022YFA1502902), the National Natural Science Foundation of China (22371208, 22271218), and the Natural Science Foundation of Tianjin City (24JCZDJC00220, 24JCYBJC00800, 23JCQNJC00570).

#### Appendix A. Supporting information

Supplementary data associated with this article can be found in the online version at doi:10.1016/j.apcatb.2025.125878.

## **Data Availability**

Data will be made available on request.

#### References

- C.L. Quéré, G.P. Peters, P. Friedlingstein, R.M. Andrew, J.G. Canadell, S.J. Davis, R. B. Jackson, M.W. Jones, Fossil CO<sub>2</sub> emissions in the post-COVID-19 era, Nat. Clim. Change 11 (2021) 197–199.
- [2] S.J. Davis, K. Caldeira, H.D. Matthews, Future CO<sub>2</sub> emissions and climate change from existing energy infrastructure, Science 329 (2010) 1330–1333.
- [3] E.A.R. Cruz, D. Nishiori, B.L. Wadsworth, N.P. Nguyen, L.K. Hensleigh, D. Khusnutdinova, A.M. Beiler, G.F. Moore, Molecular-modified photocathodes for applications in artificial photosynthesis and solar-to-fuel technologies, Chem. Rev. 122 (2022) 16051–16109.
- [4] B. Zhang, L. Sun, Artificial photosynthesis: opportunities and challenges of molecular catalysts, Chem. Soc. Rev. 48 (2019) 2216–2264.
- [5] C. Liu, B.C. Colón, M. Ziesack, P.A. Silver, D.G. Nocera, Water splittingbiosynthetic system with CO<sub>2</sub> reduction efficiencies exceeding photosynthesis, Science 352 (2016) 1210–1213.
- [6] Q.-J. Wu, J. Liang, Y.-B. Huang, R. Cao, Thermo-, electro-, and photocatalytic CO<sub>2</sub> conversion to value-added products over porous metal/covalent organic frameworks, Acc. Chem. Res. 55 (2022) 2978–2997.
- [7] L. Yang, Y.-T. Peng, X.-D. Luo, Y. Dan, J.-H. Ye, Y. Zhou, Z.-G. Zou, Beyond C<sub>3</sub>N<sub>4</sub> p-conjugated metal-free polymeric semiconductors for photocatalytic chemical transformations, Chem. Soc. Rev. 50 (2021) 2147–2172.
- [8] X.-D. Li, Y.-F. Sun, J.-Q. Xu, Y.-J. Shao, J. Wu, X.-L. Xu, P. Yang, H.-X. Ju, J.-F. Zhu, Y. Xie, Selective visible-light-driven photocatalytic CO<sub>2</sub> reduction to CH<sub>4</sub> mediated by atomically thin CuIn<sub>5</sub>S<sub>8</sub> layers, Nat. Energy 4 (2019) 690–699.
- [9] H. Wang, L. Zhang, Z. Chen, J. Hu, S. Li, Z. Wang, J. Liu, X. Wang, Semiconductor heterojunction photocatalysts: design, construction, and photocatalytic performances, Chem. Soc. Rev. 43 (2014) 5234–5244.
- [10] Y. Wang, X. Shang, J. Shen, Z. Zhang, D. Wang, J. Lin, J.C.S. Wu, X. Fu, X. Wang, C. Li, Direct and indirect Z-scheme heterostructure-coupled photosystem enabling cooperation of CO<sub>2</sub> reduction and H<sub>2</sub>O oxidation, Nat. Commun. 11 (2020) 3043.
- [11] F. Xu, K. Meng, B. Cheng, S. Wang, J. Xu, J. Yu, Unique S-scheme heterojunctions in self-assembled TiO<sub>2</sub>/CsPbBr<sub>3</sub> hybrids for CO<sub>2</sub> photoreduction, Nat. Commun. 11 (2020) 4613.
- [12] G. Lan, Y. Fan, W. Shi, E. You, S. Veroneau, W. Lin, Biomimetic active sites on monolayered metal-organic frameworks for artificial photosynthesis, Nat. Catal. 5 (2022) 1006–1018.
- [13] X. Feng, Y. Pi, Y. Song, C. Brzezinski, Z. Xu, Z. Li, W. Lin, Metal-organic frameworks significantly enhance photocatalytic hydrogen evolution and CO<sub>2</sub> reduction with earth-abundant copper photosensitizers, J. Am. Chem. Soc. 142 (2020) 690–695.
- [14] K. Sun, Y. Huang, Q. Wang, W. Zhao, X. Zheng, J. Jiang, H.-L. Jiang, Manipulating the spin state of co sites in metal-organic frameworks for boosting CO<sub>2</sub> photoreduction, J. Am. Chem. Soc. 146 (2024) 3241–3249.
- [15] N.-Y. Huang, J.-Q. Shen, X.-W. Zhang, P.-Q. Liao, J.-P. Zhang, X.-M. Chen, Coupling ruthenium bipyridyl and cobalt imidazolate units in a metal-organic framework for an efficient photosynthetic overall reaction in diluted CO<sub>2</sub>, J. Am. Chem. Soc. 144 (2022) 8676–8682.
- [16] L.-Z. Dong, L. Zhang, J. Liu, Q. Huang, M. Lu, W.-X. Ji, Y.-Q. Lan, Stable heterometallic cluster-based organic framework catalysts for artificial photosynthesis, Angew. Chem. Int. Ed. 59 (2020) 2659–2663.
- [17] A. Dhakshinamoorthy, Z. Li, S. Yang, H. Garcia, Metal-organic framework heterojunctions for photocatalysis, Chem. Soc. Rev. 53 (2024) 3002–3035.
- [18] T. Zhang, T. Li, M. Gao, W. Lu, Z. Chen, W.L. Ong, A.S.W. Wong, L. Yang, S. Kawi, G.W. Ho, Ligand mediated assembly of CdS colloids in 3D porous metal-organic framework derived scaffold with multi-sites heterojunctions for efficient CO<sub>2</sub> photoreduction, Adv. Energy Mater. 14 (2024) 2400388.
- [19] Z. Zhang, Y. Wang, Y. Xie, T. Tsukamoto, Q. Zhao, Q. Huang, X. Huang, B. Zhang, W. Song, C. Chen, H. Sheng, J. Zhao, Floatable artificial leaf to couple oxygentolerant CO<sub>2</sub> conversion with water purification, Nat. Commun. 16 (2025) 274.
- [20] L. Zhao, J. Bian, X. Zhang, L. Bai, L. Xu, Y. Qu, Z. Li, Y. Li, L. Jing, Construction of ultrathin S-scheme heterojunctions of single ni atom immobilized Ti-MOF and BiVO<sub>4</sub> for CO<sub>2</sub> photoconversion of nearly 100% to CO by pure water, Adv. Mater. 34 (2022) 2205303.
- [21] M. Zhou, H. Wang, R. Liu, Z. Liu, X. Xiao, W. Li, C. Gao, Z. Lu, Z. Jiang, W. Shi, Y. Xiong, Construction of frustrated lewis pairs in poly(heptazine imide) nanosheets via hydrogen bonds for boosting CO<sub>2</sub> photoreduction, Angew. Chem. Int. Ed. 63 (2024) e202407468.
- [22] Y.-N. Gong, J.-H. Mei, W.-J. Shi, J.-W. Liu, D.-C. Zhong, T.-B. Lu, Boosting CO<sub>2</sub> photoreduction to formate or CO with high selectivity over a covalent organic framework covalently anchored on graphene oxide, Angew. Chem. Int. Ed. 63 (2024) e202318735.
- [23] Z. Jiang, X. Xu, Y. Ma, H.S. Cho, D. Ding, C. Wang, J. Wu, P. Oleynikov, M. Jia, J. Cheng, Y. Zhou, O. Terasaki, T. Peng, L. Zan, H. Deng, Filling metal-organic

- framework mesopores with  $TiO_2$  for  $CO_2$  photoreduction, Nature 586 (2020)
- [24] L.-Y. Wu, Y.-F. Mu, X.-X. Guo, W. Zhang, Z.-M. Zhang, M. Zhang, T.-B. Lu, Encapsulating perovskite quantum dots in iron-based metal-organic frameworks (MOFs) for efficient photocatalytic CO<sub>2</sub> reduction, Angew. Chem. Int. Ed. 58 (2019) 9491–9495.
- [25] Z. Guo, G. Chen, C. Cometto, B. Ma, H.Y. Zhao, T. Groizard, L.J. Chen, H. Fan, W.-L. Man, S.-M. Yiu, K.-C. Lau, T.-C. Lau, M. Robert, Selectivity control of CO versus HCOO production in the visible-light-driven catalytic reduction of CO<sub>2</sub> with two cooperative metal sites, Nat. Catal. 2 (2019) 801–808.
- [26] W. Yang, H.-J. Wang, R.-R. Liu, J.-W. Wang, C. Zhang, C. Li, D.-C. Zhong, T.-B. Lu, Tailoring crystal facets of metal-organic layers to enhance photocatalytic activity for CO<sub>2</sub> reduction, Angew. Chem. Int. Ed. 60 (2021) 409–414.
- [27] G. Yang, S. Li, N. Li, P. Zhang, C. Su, L. Gong, B. Chen, C. Qu, D. Qi, T. Wang, J. Jiang, Enhanced photocatalytic CO<sub>2</sub> reduction through hydrophobic microenvironment and binuclear cobalt synergistic effect in metallogels, Angew. Chem. Int. Ed. 61 (2022) e202205585.
- [28] Q. Liu, Y. Song, Y. Ma, Y. Zhou, H. Cong, C. Wang, J. Wu, G. Hu, M.O. Keeffe, H. Deng, Mesoporous cages in chemically robust MOFs created by a large number of vertices with reduced connectivity, J. Am. Chem. Soc. 141 (2019) 488–496.
- [29] G. Kresse, J. Hafner, Ab initio molecular-dynamics simulation of the liquid-metalamorphous-semiconductor transition in germanium, Phys. Rev. B 49 (1994) 14251–14269.
- [30] J.P. Perdew, K. Burke, M. Ernzerhof, Generalized gradient approximation made simple, Phys. Rev. Lett. 77 (1996) 3865–3868.
- [31] P.E. Blochl, Projector augmented-wave method, Phys. Rev. B 50 (1994) 17953–17979.
- [32] M.-M. Xu, Q. Chen, L.-H. Xie, J.-R. Li, Exchange reactions in metal-organic frameworks: new advances, Coord. Chem. Rev. 421 (2020) 213421.
- [33] J. Zhu, M. Xiao, D. Ren, R. Gao, X. Liu, Z. Zhang, D. Luo, W. Xing, D. Su, A. Yu, Z. Chen, Quasi-covalently coupled Ni-Cu atomic pair for synergistic electroreduction of CO<sub>2</sub>, J. Am. Chem. Soc. 144 (2022) 9661–9671.
- [34] Y. Fan, H. Xu, G. Gao, M. Wang, W. Huang, L. Ma, Y. Yao, Z. Qu, P. Xie, B. Dai, N. Yan, Asymmetric Ru-In atomic pairs promote highly active and stable acetylene hydrochlorination, Nat. Commun. 15 (2024) 6035.
- [35] Z. Sun, C. Li, Z. Wei, F. Zhang, Z. Deng, K. Zhou, Y. Wang, J. Guo, J. Yang, Z. Xiang, P. Ma, H. Zhai, S. Li, W. Chen, Sulfur-bridged asymmetric CuNi bimetallic atom sites for CO<sub>2</sub> reduction with high efficiency, Adv. Mater. 36 (2024) 2404665.
- [36] Q. Zhou, W. Xue, X. Cui, P. Wang, S. Zuo, F. Mo, C. Li, G. Liu, S. Ouyang, S. Zhan, J. Chen, C. Wang, Oxygen-bridging fe, co dual-metal dimers boost reversible oxygen electrocatalysis for rechargeable Zn-air batteries, PNAS 121 (2024) e2404013121.
- [37] G.-Y. Qiao, D. Guan, S. Yuan, H. Rao, X. Chen, J.-A. Wang, J.-S. Qin, J.-J. Xu, J. Yu, Perovskite quantum dots encap-sulated in a mesoporous metal-organic framework as synergistic photocathode materials, J. Am. Chem. Soc. 143 (2021) 14253–14260.
- [38] X. Wang, X. Ding, Y. Jin, D. Qi, H. Wang, Y. Han, T. Wang, J. Jiang, Post-nickelation of a crystalline trinuclear copper organic framework for synergistic photocatalytic carbon dioxide conversion, Angew. Chem. Int. Ed. 62 (2023) e202302808.
- [39] Y.-N. Gong, W. Zhong, Y. Li, Y. Qiu, L. Zheng, J. Jiang, H.-L. Jiang, Regulating photocatalysis by spin-state manipulation of cobalt in covalent organic frameworks, J. Am. Chem. Soc. 142 (2020) 16723–16731.
- [40] L. Wang, B. Cheng, L. Zhang, J. Yu, In situ irradiated XPS investigation on S-scheme TiO<sub>2</sub>@ZnIn<sub>2</sub>S<sub>4</sub> photocatalyst for efficient photocatalytic CO<sub>2</sub> reduction, Small 17 (2021) 2103447.
- [41] H. Moon, K.-C. Hsiao, M.-C. Wu, Y. Yun, Y.-J. Hsu, K. Yong, Spatial separation of cocatalysts on Z-scheme organic/inorganic heterostructure hollow spheres for enhanced photocatalytic H<sub>2</sub> evolution and In-depth analysis of the charge-transfer mechanism, Adv. Mater. 35 (2023) 2200172.
- [42] M.-L. Xu, M. Lu, G.-Y. Qin, X.-M. Wu, T. Yu, L.-N. Zhang, K. Li, X. Cheng, Y.-Q. Lan, Piezo-photocatalytic synergy in BiFeO<sub>3</sub>@COF Z-scheme heterostructures for highefficiency overall water splitting, Angew. Chem. Int. Ed. 61 (2022) e202210700.
- [43] L. Wang, Y. Li, Y. Ai, E. Fan, F. Zhang, W. Zhang, G. Shao, P. Zhang, Tracking heterogeneous interface charge reverse separation in SrTiO<sub>3</sub>/NiO/NiS nanofibers with in situ irradiation XPS, Adv. Funct. Mater. 33 (2023) 2306466.

- [44] Y.-F. Xu, M.-Z. Yang, B.-X. Chen, X.-D. Wang, H.-Y. Chen, D.-B. Kuang, C.-Y. Su, A CsPbBr<sub>3</sub> perovskite quantum dot/graphene oxide composite for photocatalytic CO<sub>2</sub> reduction, J. Am. Chem. Soc. 139 (2017) 5660–5663.
- [45] P. Dong, X. Xu, R. Luo, S. Yuan, J. Zhou, J. Lei, Postsynthetic annulation of threedimensional covalent organic frameworks for boosting CO<sub>2</sub> photoreduction, J. Am. Chem. Soc. 145 (2023) 15473–15481.
- [46] Y. Liu, C.-H. Liu, T. Debnath, Y. Wang, D. Pohl, L.V. Besteiro, D.M. Meira, S. Huang, F. Yang, B. Rellinghaus, M. Chaker, D.F. Perepichka, D. Ma, Silver nanoparticle enhanced metal-organic matrix with interface-engineering for efficient photocatalytic hydrogen evolution, Nat. Commun. 14 (2023) 541.
- [47] F. Roth, M. Borgwardt, L. Wenthaus, J. Mahl, S. Palutke, G. Brenner, G. Mercurio, S. Molodtsov, W. Wurth, O. Gessner, W. Eberhardt, Direct observation of charge separation in an organic light harvesting system by femtosecond time-resolved XPS, Nat. Commun. 12 (2021) 1196.
- [48] J.T. DuBose, P.V. Kamat, How pendant groups dictate energy and electron transfer in perovskite-rhodamine light harvesting assemblies, J. Am. Chem. Soc. 145 (2023) 4601–4612.
- [49] J. Li, H. Huang, W. Xue, K. Sun, X. Song, C. Wu, L. Nie, Y. Li, C. Liu, Y. Pan, H.-L. Jiang, D. Mei, C. Zhong, Self-adaptive dual-metal-site pairs in metal-organic frameworks for selective CO<sub>2</sub> photoreduction to CH<sub>4</sub>, Nat. Catal. 4 (2021) 719–729.
- [50] G. Wang, Y. Wu, Z. Li, Z. Lou, Q. Chen, Y. Li, D. Wang, J. Mao, Engineering a copper single-atom electron bridge to achieve efficient photocatalytic CO<sub>2</sub> conversion, Angew. Chem. Int. Ed. 62 (2023) e202218460.
- [51] Z. Li, J.-D. Xiao, H.-L. Jiang, Encapsulating a Co(II) molecular photocatalyst in metal-organic framework for visible-light-driven H<sub>2</sub> production: boosting catalytic efficiency via spatial charge separation, ACS Catal. 6 (2016) 5359–5365.
- [52] J.-S. Zhao, Y.-F. Mu, L.-Y. Wu, Z.-M. Luo, L. Velasco, M. Sauvan, D. Moonshiram, J.-W. Wang, M. Zhang, T.-B. Lu, Directed electron delivery from a Pb-free halide perovskite to a Co(II) molecular catalyst boosts CO<sub>2</sub> photoreduction coupled with water oxidation, Angew. Chem. Int. Ed. 63 (2024) e202401344.
- [53] K. Yuan, K. Tao, T. Song, Y. Zhang, T. Zhang, F. Wang, S. Duan, Z. Chen, L. Li, X. Zhang, D. Zhong, Z. Tang, T.-B. Lu, W. Hu, Large-area conductive MOF ultrathin film controllably integrating dinuclear-metal sites and photosensitizers to boost photocatalytic CO<sub>2</sub> reduction with H<sub>2</sub>O as an electron donor, J. Am. Chem. Soc. 146 (2024) 6893–6904.
- [54] T.-C. Zhuo, Y. Song, G.-L. Zhuang, L.-P. Chang, S. Yao, W. Zhang, Y. Wang, P. Wang, W.-B. Lin, T.-B. Lu, Z.-M. Zhang, H-bond-mediated selectivity control of formate versus CO during CO<sub>2</sub> photoreduction with two cooperative Cu/X sites, J. Am. Chem. Soc. 143 (2021) 6114–6122.
- [55] J.-W. Wang, L.-Z. Qiao, H.-D. Nie, H.-H. Huang, Y. Li, S. Yao, M. Liu, Z.-M. Zhang, Z.-H. Kang, T.-B. Lu, Facile electron delivery from graphene template to ultrathin metal-organic layers for boosting CO<sub>2</sub> photoreduction, Nat. Commun. 12 (2021) 813
- [56] Z. Wu, H. Wu, W. Cai, Z. Wen, B. Jia, L. Wang, W. Jin, T. Ma, Engineering bismuthtin interface in dual-metal aerogel with a 3D porous structure for highly selective electrocatalytic CO<sub>2</sub> reduction to HCOOH, Angew. Chem. Int. Ed. 60 (2021) 12554–12559
- [57] G. Ruan, P. Ghosh, N. Fridman, G. Maayan, A di-copper-peptoid in a noninnocent borate buffer as a fast electrocatalyst for homogeneous water oxidation with low overpotential, J. Am. Chem. Soc. 143 (2021) 10614–10623.
- [58] Z. Wu, F. Ye, Q. Liu, R. Pang, Y. Liu, L. Jiang, Z. Tang, L. Hu, Simultaneous incorporation of v and mn element into polyanionic NASICON for high energydensity and long-lifespan Zn-Ion storage, Adv. Energy Mater. 12 (2022) 2200654.
- [59] J.-W. Wang, K. Yamauchi, H.-H. Huang, J.-K. Sun, Z.-M. Luo, D.-C. Zhong, T.-B. Lu, K. Sakai, A molecular cobalt hydrogen evolution catalyst showing high activity and outstanding tolerance to CO and O<sub>2</sub>, Angew. Chem. Int. Ed. 58 (2019) 10923–10927.
- [60] H. Wang, T. Zhai, Y. Wu, T. Zhou, B. Zhou, C. Shang, Z. Guo, High-Valence oxides for high performance oxygen evolution electrocatalysis, Adv. Sci. 10 (2023) 2301706
- [61] Q. Yu, Theoretical studies of non-noble metal single-atom catalyst Ni<sub>1</sub>/MoS<sub>2</sub>: electronic structure and electrocatalytic CO<sub>2</sub> reduction, Sci. China Mater. 66 (2023) 1079–1088.